END

MICROCOPY RESOLUTION TEST CHART

NATIONAL BUREAU OF STANDARDS-1963-A

⑤

REPORT DOCUMENTATION PAGE	READ INSTRUCTIONS BEFORE COMPLETING FORM

1 REPORT NUMBER	2 GOVT ACCESSION NO.	3 RECIPIENT'S CATALOG NUMBER
AFOSR-TR- 84-0882		

4. TITLE *(and Subtitle)*	5. TYPE OF REPORT & PERIOD COVERED
Thermodynamics of High Temperature Materials	Final Report 10/1/82 - 09/30/83
	6 PERFORMING ORG. REPORT NUMBER

7. AUTHOR(s)	8. CONTRACT OR GRANT NUMBER(s)
Abramowtiz, Stanley (Dr.)	AFOSR-ISSA-83-00038

9. PERFORMING ORGANIZATION NAME AND ADDRESS	10 PROGRAM ELEMENT, PROJECT, TASK AREA & WORK UNIT NUMBERS
National Bureau of Standards Center for Chemical Physics Gaithersburg, MD 20899	2306/A2 61102F 2306/K1

11. CONTROLLING OFFICE NAME AND ADDRESS	12. REPORT DATE
AFOSR/NE Bolling, AFB DC 20332	September 1988
	13. NUMBER OF PAGES 78

14 MONITORING AGENCY NAME & ADDRESS(*if different from Controlling Office*)	15. SECURITY CLASS. *(of this report)*
	UNCLASSIFIED
	15a. DECLASSIFICATION DOWNGRADING SCHEDULE

AD-A147 725

16 DISTRIBUTION STATEMENT *(of this Report)*

Approved for public release;
distribution unlimited.

17 DISTRIBUTION STATEMENT *(of the abstract entered in Block 20, if different from Report)*

DTIC
ELECTE
NOV 23 1984
E

18 SUPPLEMENTARY NOTES

are

19 KEY WORDS *(Continue on reverse side if necessary and identify by block number)*
Thermodynamics, High Temperature Materials, Carbon, Silicon Nitride, Graphite, Thermophysics, Carbon Chains, Ablation, Graphite Layers, Chemical Kinetics, Vaporization, Refractory Materials.

20 ABSTRACT *(Continue on reverse side if necessary and identify by block number)*
High temperature thermophysical behavior of model systems of importance to high temperature phenomena including carbon and silicon nitride studied. Kinetics of evaporation of refractory materials subjected to laser irradiation studied. Study of thermodynamic effects of melastic collisons conducted. results compared to JANAF Tables. Kinetics of gas phase ionic reaction mechanisms leading to build up of a long chain unsaturated carbon species studied. Basic chemical steps involved in formation and decomposition of graphitic layers explored.

DD FORM 1473   EDITION OF 1 NOV 65 IS OBSOLETE
1 JAN 73

UNCLASSIFIED

84 10 23 194   SECURITY CLASSIFICATION OF THIS PAGE *When Data Entered*

DTIC FILE COPY

Thermodynamics of High Temperature Materials

Final Report for the Period

1 October 1982 - 30 September 1983

AIR FORCE OFFICE OF SCIENTIFIC RESEARCH

AFOSR-ISSA-83-00038

Accession For	
NTIS GRA&I	☒
DTIC TAB	☐
Unannounced	☐
Justification	
By	
Distribution/	
Availability Codes	
Dist	Avail and/or Special
A-1	

TABLE OF CONTENTS

ABSTRACT

The research described encompasses eight tasks each of which treats, from either an experimental or theoretical base, the measurement or interpretation of the high-temperature thermophysical behavior of model systems which show potential applicability to the protection of spacecraft from directed energy beams. The Spacecraft Survivability research initiative aadresses such areas as the high temperature thermophysical properties of model structural and/or shield materials; the generation and dispersal of smokes and obscuring materials in space; the kinetics of evaporation of refractory materials under laser irradiation and their subsequent condensation leading to the formation of microscopic particles and; the thermophysical properties of high temperature polyatomic gas phase species. Since carbon is a likely candidate material for a protective coating, many of the efforts deal with graphite or other carbon containing materials.

The optimum sample configuration and gaseous environment for pulse-heating measurements on graphite near its triple point ($\sim$ 4700 K, 11 MPa) have been investigated. A limited number of heat-capacity measurements on AXM-5Q1 Poco graphite were carried out between 1900 and 3000 K. A new pulse-interferometric technique was used to study the linear thermal expansion of iron in the vicinity of its fcc-bcc phase transformation. The relative enthalpies of α- and β-Si_3N_4 were measured with a drop calorimeter in the temperature range 273-1173 K. The thermodynamic effects of inelastic collisions have been rigorously analyzed in a detailed critique of conventional calculational methods (such as used in the JANAF Tables) which employ spectroscopic data in the evaluation of thermodynamic properties at elevated temperatures. Both inelastic coupling and predissociation effects are shown to be negligible. As part of an attempt to elucidate the basic chemical steps involved in the formation and decomposition of large-scale graphitic molecules, it has been shown practical to apply available π-electron theories originally derived for benzenoid systems to very large, well-defined graphitic planes.

The kinetics of gas-phase ionic reaction mechanisms leading to the build-up of long polyunsaturated carbon chain ions under near-vacuum conditions in hydrogen-deficient systems have been investigaetd using the NBS ion cyclotron resonance spectrometer. Hardware development of the measurement system is

outlined. Experimental results are presented for the systems diacetylene and cyanoacetylene. Laser ablation studies of graphite surfaces followed by mass-spectrometric examination of the plume constituent species were carried out. The free-jet expansion method of cluster formation in the gas phase was tested using KCl vapor species.

1. A Study of the Behavior of Graphite in the Temperature Range 3600 K to its Triple Point under Rapid Pulse Heating Conditions

A. Cezairliyan, A. P. Miiller, and J. L. McClure

Among refractory materials, graphite is one of the most important for technological applications at high temperatures, particularly in areas such as rocketry and spacecraft. As yet however, there have been only a limited number of accurate measurements on the thermal properties of graphite above 1500 K reported in the literature. The relatively few investigations above 3000 K have yielded data which are in considerable disagreement.

As part of a continuing program to obtain accurate data on selected thermophysical properties of graphite at high temperatures, the heat capacity and electrical resistivity of two grades of graphite (Poco DFP-2 and Poco AXF -9Q1) were measured at temperatures in the range 2500 to 3600 K, and the results were presented in the previous report [1]. The experiments were performed by means of a rapid pulse-heating technique [2,3] with the specimen in a pressurized gas (argon) environment at 4 MPa ($\sim$ 40 atm). A comparison of the results with those reported earlier for the same grades of graphite in the range 1500 to 3000 K [4] shows that they are in good agreement (about 1% on average) at all temperatures common to both investigations. In the more recent study, however, the high vapor pressure of graphite became the major limiting problem: interference by specimen vapor (in the form of soot) with thermal radiation from the specimen prevented accurate pyrometric measurements above about 3600 K.

The objective of the present study is to determine those experimental conditions necessary to suppress or, at least, minimize the effect of specimen evaporation so that pyrometric measurements of specimen temperature can be extended to significantly higher temperatures, perhaps even above the triple point temperature of graphite. This work should provide invaluable baseline data for future experiments on the heat capacity of graphite at temperatures approaching the triple point.

The present study required two major changes to the existing pulse heating system: (1) the addition of an ultra-high pressure cell in which the specimens could be pulse heated in a gas environment at pressures up to 200 MPa ($\sim$ 2000 atm) and (2) the construction of a single wavelength (0.65 μm) photoelectric pyrometer capable of measuring the specimen radiance at a rate as high as one measurement every 50 μs. In all pulse experiments described below, the measurements with the pyrometer yielded only the radiance or brightness temperature of the specimen surface. Unless mentioned otherwise, all experiments were conducted with the specimens in a pressurized argon atmosphere at 120 MPa ($\sim$ 1200 atm). This pressure is significantly above the values of triple point pressure reported in the literature (10-12 MPa).

The initial series of tests were performed on graphite specimens in the form of solid cylindrical rods with nominal dimensions of 40 mm long by 3 mm in diameter. Each specimen, in turn, was rapidly heated from room temperature to the temperature of interest by the passage of an electrical current pulse ($\sim$ 350 ms duration) through it. Heating rates in these tests were similar to those used in the earlier work [1], that is, of the order of 10^4 K$\cdot$s^{-1}. The results of a typical pulse experiment are presented in Fig. 1(a) which illustrates the variation in time of the surface radiance temperature, as seen by the pyrometer, and the current through the specimen. The heating curve (radiance temperature versus time) is essentially smooth up to about 3800 K (corresponds to a true temperature of about 3900 K if one assumes the normal spectral emittance $\varepsilon_{0.65}$ of the specimen surface to be in the range 0.8-0.9). Above 3800 K, however, the curve shows discontinuities typical of interference of graphite vapor with radiation from the specimen.

The second series of tests were conducted on smaller cylindrical specimens (length, 12 mm; diameter, 1.5 mm), resulting in a significant increase in the heating rate to about 10^5 K$\cdot$s^{-1}. As can be seen in Fig. 1(b), the surface radiance temperature increases smoothly to about 4100 K before the onset of specimen evaporation. The apparent oscillations in the surface radiance (seen as discontinuities in slower experiments described above) are believed to be the result of rapid evaporation and re-condensation of graphite vapor at the specimen surface, at sufficiently

high temperatures. Evidence of condensed graphite vapor or soot can be seen in Fig. 2(a) which presents a photograph of a specimen taken after pulse heating.

In order to further reduce specimen volume, a number of graphite specimens were fabricated into the form of small rectangular strips, each with a "necked-down" portion at its center forming an "effective" specimen. The dimensions of the effective specimen were nominally: length, 2 mm; width, 1 mm; thickness, 0.5 mm. For pulse experiments on the strip specimens, heating rates were typically about 2×10^5 K·s^{-1}. After each pulse heating experiment, an examination of the effective portion of the specimen revealed strong evidence of melting as manifested by some glassy areas on the (effective) specimen surface. Unfortunately, the onset of specimen evaporation prior to melting limited the measurements of radiance temperature to below about 4200 K.

Finally, a number of strip specimens were pulse heated in an argon gas environment at 20 MPa containing a small amount of oxygen (10 to 30%). As anticipated, the oxygen combined with the graphite vapor to form CO and CO_2 thereby eliminating the formation of graphite soot. As can be seen in Fig. 2(b), the surface of the remaining portion of effective specimen is glassy without any evidence of condensed graphite vapor. Furthermore, the radiance temperature rises smoothly until a melting plateau is reached as shown in Fig. 3(a); the plateau corresponds to a radiance temperature of about 4500 K. Figure 3(b) gives a comparison of melting plateaus obtained in three successive experiments in which the oxygen content in the gas environment was approximately 10, 20 and 30%. The maximum spread in radiance temperatures among the plateaus is about 25 K.

The value of true temperature corresponding to the melting plateau, of course, depends on the value of $\varepsilon_{0.65}$ of the surface. For graphite, $\varepsilon_{0.65}$ is expected to be in the range 0.9 to 0.8 which yields a corresponding melting temperature in the range of about 4600 to 4700 K. These values are within the wide spread in melting temperatures (about 4000 to 4900 K) reported in the literature [5].

In summary, the present study has shown that, by increasing the gas environment pressure and/or the heating rate, the evaporation of the

graphite specimen during pulse heating can be suppressed and/or retarded until significantly higher temperatures are reached. Also, the addition of a small amount of oxygen appears to remove the graphite soot in the vicinity of the specimen surface thereby permitting the pyrometric measurement of temperature up to the melting point of the specimen. Furthermore, this study shows that, in order to achieve the desired heating rates with the present pulse heating system, the volume of the effective specimen must be relatively small. This requirement virtually eliminates any consideration of tubular specimen geometries (with a blackbody sighting hole), as used in earlier studies [1,4], for accurate measurements of thermal properties above about 4000 K. Consequently plans are underway to construct a multi-wavelength pyrometer so that true temperatures can be determined directly from measurements of surface radiance at two or more wavelengths.

References

1. A. Cezairliyan, A.P. Miiller, and M.S. Morse, in the 1981 Annual Report to the Air Force Office of Scientific Research, AFOSIR-ISSA-81-00012.
2. A. Cezairliyan, J. Res. Nat. Bur. Stand. (U.S.) 75C, 7 (1971).
3. A. Cezairliyan, M.S. Morse, H.A. Berman, and C.W. Beckett, J. Res. Nat. Bur. Stand. (U.S.) 74A, 65 (1970).
4. A. Cezairliyan and F. Righini, Rev. Int. Htes. Temp. et Réfract. 12, 124 (1975).
5. N.A. Gokcen, E.T. Chang, T.M. Poston, and D.J. Spencer, Report SAMSO-TR-76-29.

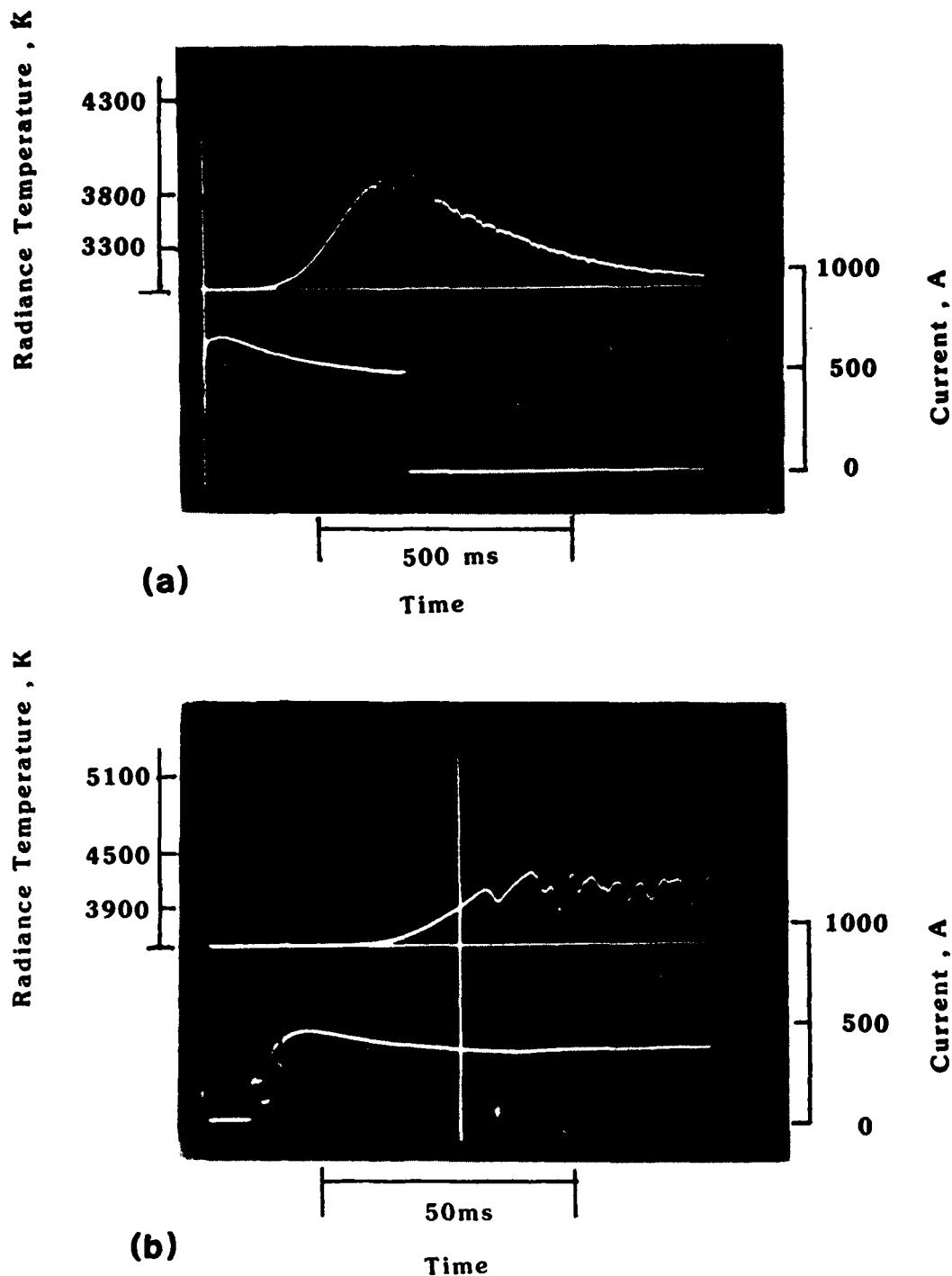**Fig. 1** Oscilloscope trace photographs showing the variation with time of the radiance temperature of the specimen surface, as seen by the pyrometer, and the current through the specimen during typical experiments in which the specimens were pulse heated in a pressurized gas (argon) environment at 120 MPa (about 1200 atm) and at heating rates of about (a) 10^4 K·s^{-1} and (b) 10^5 K·s^{-1}.

(a)
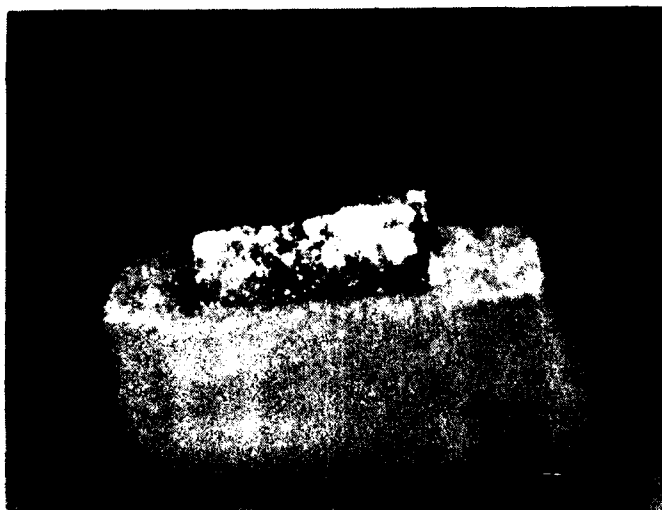
(b)

Fig. 2   Photographs of the specimen surface after pulse heating.
(a) The surface of a cylindrical specimen, pulse heated in a
pure argon environment at 120 MPa, shows evidence of recondensed
graphite vapor in the form of soot. (b) The glassy appearance
of the surface of a strip specimen, pulse heated in a mixed
gas (90% argon, 10% oxygen) environment at 20 MPa, provides
strong evidence that melting has occurred.
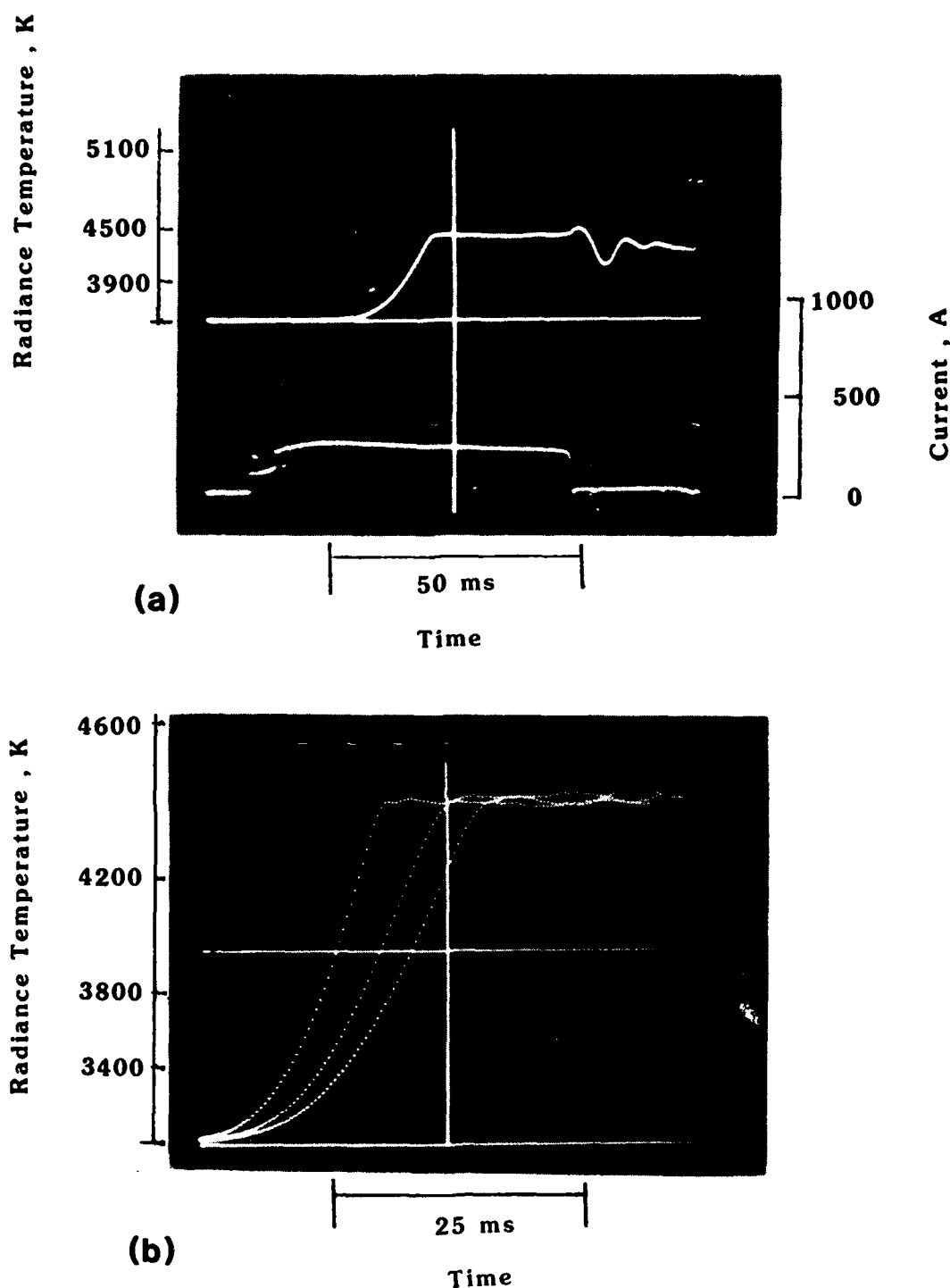
Fig. 3 Oscilloscope trace photographs showing the results of experiments in which strip specimens were pulse heated in a pressurized argon gas environment (at 20 MPa) containing small amounts of oxygen (10-30%). (a) The plateau in the radiance temperature versus time curve indicates that melting of the graphite specimen has occurred. (b) A comparison of melting plateaus that were obtained from three experiments, in which strip specimens were pulse heated in pressurized argon containing 10%, 20% and 30% oxygen, shows no significant difference.

2. <u>Heat Capacity of AXM-5Q1 Poco Graphite for the CODATA Program by</u>
    <u>a Pulse Heating Technique (Limited Measurements)</u>
    A. Cezairliyan, A. P. Miiller, and M. S. Morse

Recent measurements of heat capacity of AXM-5Q1 Poco graphite by
Righini et al. [1] at the Instituto di Metrologia "G. Colonetti" (IMGC)
have yielded results that are systematically lower by about 2 to 3% than
those obtained earlier by Cezairliyan [2] at the National Bureau of
Standards (NBS), for a similar grade (AXM-5Q) of graphite. This difference,
while within the combined uncertainty (7%) of the two investigations, is
considerably larger than the measurement resolution ($\sim$0.5%) of the
pulse-heating methods (identical in principle) used at the two laboratories.
In order to elucidate possible sources of this difference, the specimen
used by Righini et al. was made available to NBS for further measurements.
The results of these measurements are described herein.

In order to accommodate the tubular specimen from IMGC inside the
experiment chamber at NBS, the length of the specimen was reduced by
approximately 25 mm. The dimensions of the specimen, as used in our
measurements, are given in Table 1 along with other pertinent physical
properties of the specimen. The reduction in specimen length does not
significantly deteriorate the blackbody quality of the pyrometric
sighting hole. Therefore, the value 0.994 estimated by Righini et al.
was used for our computation of specimen temperature throughout the
present work.

The specimen was pulse-heated in a vacuum environment ($\sim$1 mPa),
successively from room temperature through four overlapping temperature
ranges between 1900 and 3000 K. During each pulse experiment, simultaneous
measurements of the specimen temperature, the voltage across, and the
current through the specimen were recorded with millisecond time resolution.
The duration of the electrical current pulse, used to resistively heat
the specimen, varied between 380 and 690 ms.

The heat capacity was computed from data taken during the heating
period. Corrections were made for the radiative heat loss from the
specimen based on data taken during the initial free cooling period of
the specimen. The function that represents the results for heat capacity

. (standard deviation = 0.2%) in the temperature range 1900 to 3000 K is:

$$C_p = 19.36 + 4.005 \times 10^{-3} \, T - 5.539 \times 10^{-7} \, T^2$$

where C_p is in $J \cdot mol^{-1} \cdot K^{-1}$ and T is in K.

The electrical resistivity of the AXM-5Q1 Poco graphite specimen was determined from the same experiments that were used to calculate heat capacity. The function that represents the results for electrical resistivity (standard deviation = 0.1%) in the temperature range 1900 to 3000 K is:

$$\rho = 1299.9 - 0.37247T + 2.2451 \times 10^{-4} \, T^2 - 3.1144 \times 10^{-8} \, T^3$$

where ρ is in $\mu\Omega \cdot cm$ and T is in K.

In Table 2, we present a comparison of our results for heat capacity and electrical resistivity with those obtained in measurements by Righini et al. [1] on (essentially) the same specimen of AXM-5Q1 Poco graphite. The present results are higher than those from IMGC by about 2% for electrical resistivity and by about 2-3% for heat capacity. The difference in resistivity values arises, in part, from the larger (0.6%) cross-sectional area used in our computation of electrical resistivity.

The heat capacity values obtained by the present work and by Righini et al. for the AXM-5Q1 graphite specimen are compared with results reported earlier by Cezairliyan [2] for AXM-5Q Poco graphite, in Figure 1 and in Table 3. The present results lie about 0.2-0.4% lower than those of Cezairliyan whereas, as mentioned earlier, the heat capacity data of Righini et al. lie about 2-3% lower.

Several other collateral measurements performed at NBS on different grades of Poco graphite [3,4] have yielded heat capacity values that lie within about 0.5% of the earlier results by Cezairliyan for AXM-5Q. This suggests that the "low" values of heat capacity for Poco graphite obtained by Righini et al. are not the result of differences in graphite grades or in specimen fabrication but rather, may be the result of system-related differences between the pulse heating equipment at the two laboratories. Further comparative experiments on the same specimen(s) of a selected material (molybdenum SRM 781, perhaps) are needed to determine the source of any systematic differences.

It should be noted that the measurements at NBS on AXM-5Q1
Poco graphite were intended only as a "spot-check". More complete
measurements on more than one graphite specimen in the temperature range
1500-3000 K will be performed during the next year.

References

[1] R. Righini, A. Cibrario and A. Rosso, Rapporto Interno 5/173, Instituto
    di Metrologia "G. Colonnetti", (1979).

[2] A. Cezairliyan, Proceedings of the Sixth Symposium on Thermophysical
    Properties, P.E. Liley, ed. (ASME, New York, 1973), p.279.

[3] A. Cezairliyan and F. Righini, Rev. Int. Htes Temp. et Réfract.,
    12, 124 (1975).

[4] A. Cezairliyan and J.L. McClure, Annual Report to U.S. Air Force
    Office of Scientific Research, 1981.

Table 1 - Geometrical and physical properties
of the specimen of Poco graphite
(grade AXM-5Q1)

Total length	7.6124 cm
Effective[a] length	2.5705 cm
Outside diameter[b]	0.6445 cm
Cross-sectional area	0.1560 cm^2
Effective[a] surface area	5.1478 cm^2
Total mass	2.0265 g
Effective[a] mass	0.6843 g
Atomic Weight	12.011 g·mol^{-1}
Density[b]	1.706 g·cm^{-3}
Pyrometric sighting hole dimensions[b]	1 x 1.7 mm
Blackbody quality[b]	0.994

[a] "Effective" refers to the central portion of the specimen between two grooves used to locate the voltage (knife-edge) probes.

[b] Properties or quantities as given by Righini et al. [1].

Table 2. Comparison of results obtained for the heat capacity
and electrical resistivity of AXM-5Q1 Poco graphite in
measurements carried out at IMGC and at NBS

Temperature, K	C_p, $J \cdot mol^{-1} \cdot K^{-1}$			ρ $\mu\Omega \cdot cm$		
	IMGC	NBS	Percent Difference	IMGC	NBS	Percent Difference
1900	24.48	24.97	2.0	1169.1	1189.2	1.7
2400	25.19	25.78	2.3	1247.9	1268.6	1.6
2900	25.55	26.32	2.9	1323.1	1348.3	1.9

Table 3. Comparison of heat capacity values obtained for similar grades of Poco graphite

Temperature, K	Heat capacity, $J \cdot mol^{-1} \cdot K^{-1}$		
	AXM-5Q[a] NBS	AXM-5Q1[b] IMGC	AXM-5Q1[c] NBS
1400		23.40	
1500	24.14	23.65 (-2.0%)[d]	
1600	24.38	23.88 (-2.0%)	
1700	24.61	24.09 (-2.1%)	
1800	24.83	24.29 (-2.2%)	
1900	25.03	24.48 (-2.2%)	24.97 (-0.2%)[d]
2000	25.22	24.65 (-2.3%)	25.15 (-0.3%)
2100	25.41	24.80 (-2.4%)	25.33 (-0.3%)
2200	25.57	24.95 (-2.4%)	25.49 (-0.3%)
2300	25.73	25.08 (-2.5%)	25.64 (-0.3%)
2400	25.88	25.19 (-2.7%)	25.78 (-0.4%)
2500	26.01	25.29 (-2.8%)	25.91 (-0.4%)
2600	26.13	25.38 (-2.9%)	26.03 (-0.4%)
2700	26.24	25.45 (-3.0%)	26.14 (-0.4%)
2800	26.34	25.51 (-3.2%)	26.23 (-0.4%)
2900	26.43	25.55 (-3.3%)	26.32 (-0.4%)
3000	26.50		26.39 (-0.4%)

[a]Smoothed results obtained by Cezairliyan [2] for two specimens with an estimated blackbody quality of 0.98.

[b]Smoothed results obtained by Righini et al. [1] for a specimen with an estimated blackbody quality of 0.994.

[c]Smoothed results obtained in the present measurements on the specimen used by Righini et al. after reducing its length to fit the pulse heating system at NBS.

[d]Percent deviation of the results obtained for AMX-5Q1 Poco graphite at IMGC and at NBS from results obtained earlier at NBS in measurements on a similar grade of Poco graphite (AXM-5Q).
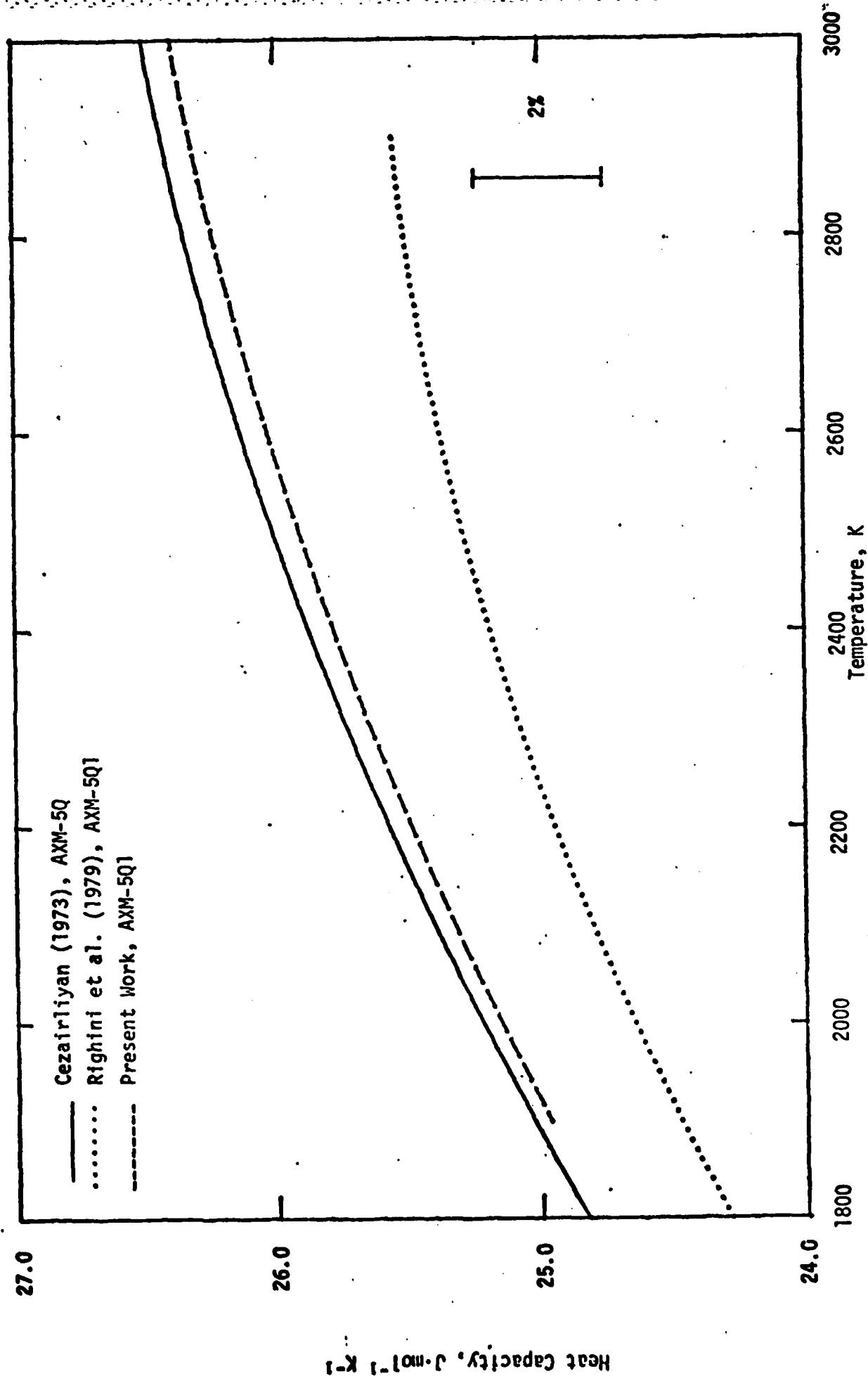
Figure 1. Comparisons of the results on heat capacity of Poco graphite.

Legend (within plot):
Cezairliyan (1973), AXM-5Q
Righini et al. (1979), AXM-5Q1
Present Work, AXM-5Q1

X-axis: Temperature, K
Y-axis: Heat capacity, J·mol⁻¹ K⁻¹

14

3. Thermal Expansion of Iron During the α → γ Phase Transformation by a Pulse Interferometric Technique

A. P. Miiller, A. Cezairliyan, and M. S. Morse

The thermal expansion of iron is of particular interest because of a unique sequence of solid-solid phase transformations: as temperature is increased, the lattice changes from a body-centered cubic to a face-centered cubic structure (α→γ) at about 1190 K and then, at a somewhat higher temperature (∼1600 K), returns to the body-centered cubic structure (γ→δ). In the present work, measurements of linear thermal expansion of iron in the vicinity of the α→γ transformation were undertaken with the purpose of establishing the applicability of the recently-developed transient interferometric technique [1] to the study of thermal expansion during rapid solid-solid phase transformations.

The basic method involves rapidly heating the specimen from room temperature to the maximum temperature of interest in less than one second by the passage of an electrical current pulse through it, and simultaneously measuring the specimen temperature by means of a high-speed photoelectric pyrometer [2] and the shift in the fringe pattern produced by a two-beam interferometer. The polarized beam from a He-Ne laser in the interferometer is split into two component beams, one which undergoes successive reflections from optical flats on opposite sides of the specimen, and one which serves as the reference beam. The linear thermal expansion of the specimen is determined from the cumulative fringe shift corresponding to a given temperature.

For the present study, three specimens were fabricated from a polycrystalline rod (nominally 99.95% pure iron) into the form of long rectangular rods with nominal dimensions: 2.4 x 4.2 x 24 mm long; the specimen "length" for the interferometric measurements corresponds to the 4.2 mm dimension. Two opposite sides of each specimen were polished to an optical flatness of better than λ/4 across the center portions.

Each specimen was pulse-heated in a vacuum environment of about 1.3 mPa (∼10^{-5} torr) from room temperature, through the α-γ transformation, to about 1300 K by passing an electrical current pulse of 750 ms duration through it. During the experiment, the analog signals from the pyrometer and the interferometer were simultaneously recorded with submillisecond time resolution by means of digital storage oscilloscopes.

Figure 1 presents three photographs of the interferometer signal as recorded during a typical pulse heating of iron through the $\alpha \rightarrow \gamma$ transformation; each cycle of the signal corresponds to the shift of one fringe or specimen expansion (contraction) of $\lambda/2$. The photographs show the reversal in direction of the fringe shifts at the onset of the $\alpha \rightarrow \gamma$ transformation, again at the completion of the transformation, and finally at the end of the pulse heating period. The sinusoidal nature of the signal remains clearly visible throughout the transformation, even near the mid-point where the amplitude is significantly reduced. The rapid change in signal amplitude is probably related to the transformation kinetics associated with the transitory formation and movement of interphase "dislocation" boundaries at the specimen surface.

The true temperature of each specimen was determined from the measured surface radiance temperature by selecting the "effective" normal spectral emittance ϵ_λ that would yield the correct transformation temperature at the arrest in the temperature-time function. The "correct" transformation temperature was selected to be 1190 K on the basis of data reported in the literature [3,4,5]. The "effective" value of ϵ_λ was assumed to remain constant for our computation of (true) temperatures throughout the range 1130-1330 K.

Values of linear thermal expansion were determined from the recorded fringe shifts and correlated with the measurements of specimen temperature. The final results were obtained by a least-squares fit to the combined thermal expansion values for the three specimens. The results at temperatures in ranges 1130-1180 K (α-phase) and 1200-1330 K (γ-phase) are expressed by the relations

$$\Delta \ell / \ell_0 = -3.778 \times 10^{-3} + 1.480 \times 10^{-5} \ T$$

and

$$\Delta \ell / \ell_0 = -1.883 \times 10^{-2} + 2.437 \times 10^{-5} \ T$$

respectively, where T is in K and ℓ_0 is the specimen "length" at 20°C.

The major source of error in the present study arises from the measurement of temperature. The maximum error is estimated to be about 16 K (α-phase) and 14 K (γ-phase) which correspond to errors in $\Delta \ell / \ell_0$ of approximately 2% and 3%, respectively. The uncertainty in the "room temperature" length ℓ_0 also contributes an error in $\Delta \ell / \ell_0$, of about 0.7%. The fringe shift count is believed to be accurate to within

0.5 fringe which corresponds to an additional error in $\Delta\ell/\ell_0$ of approximately 0.3%. Therefore, the maximum error in the reported values of linear thermal expansion is estimated to be about 4%.

The results of the present work are compared graphically in Fig. 2 with values of linear thermal expansion reported in the literature. Austin and Pierce [3], using Fizeau interferometry, observed considerable differences (∿30%) in expansion among specimens of iron from several different sources; results for one of the "purest" specimens, taken during the heating cycle of their experiment, are illustrated in Fig. 2 by open circles. The solid symbols represent expansion values as determined from the x-ray diffraction data reported by Basinski et al. [4], Gorton et al. [6] and Kohlhass et al. [7] for iron samples of high purity (99.97, 99.67 and 99.97%, respectively). The values of thermal expansion reported by Richter [5] for 99.98% pure iron were obtained by push-rod dilatometry; only data taken during the heating cycle are shown (open triangles).

From the results shown in Fig. 2, it is evident that the α-iron data of Kohlhass et al. may be in error by perhaps as much as 20%. However, the agreement among the other data, including our results, lies well with the combined experimental error of the different investigations. A comparison of expansion values determined from length changes in bulk specimens (interferometry, push-rod dilatometry) with values obtained from changes in lattice spacings (x-ray diffractometry) reveals no apparent bias with respect to measurement technique.

In conclusion, the results of the present study demonstrate the applicability of the high-speed interferometric technique to the measurement of thermal exansion during rapid solid-solid phase transformations. In future experiments, each specimen will be fabricated in the form of a precision machined tube (with optical flats) containing a small sighting hole for direct pyrometric measurement of the blackbody temperature. This will significantly reduce the uncertainty in measuring the specimen temperature and so, permit a more accurate determination of the linear thermal expansion of the specimen.

References

1. A. P. Miiller and A. Cezairliyan, International Journal of Thermophysics $\underline{3}$, 259 (1982).

2. G. M. Foley, Rev. Sci. Instrum. $\underline{41}$, 827 (1970).

3. J. B. Austin and R. H. H. Pierce, Jr., Trans. Amer. Soc. for Metals $\underline{22}$, 447 (1934).

4. Z. S. Basinski, W. Hume-Rothery and A. L. Sutton, Proc. Roy. Soc. (London) $\underline{229}$, 459 (1955).

5. V. F. Richter, Archiv Für Das Eisenhüttenwesen $\underline{41}$, 709 (1970).

6. A. T. Gorton, G. Bitsianes and T. L. Joseph, Trans. Met. Soc. AIME $\underline{233}$, 1519 (1965).

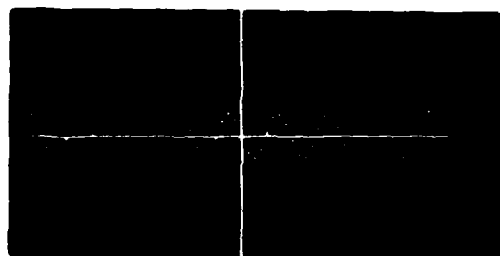7. R. Kohlhaas, Ph. Dunner and N. Schmitz-Pranghe, Zeit. Ang. Phys. $\underline{23}$ 245 (1967).

Interferometer Signal
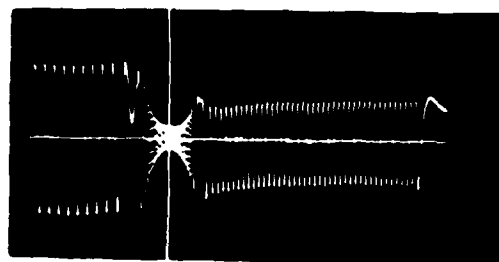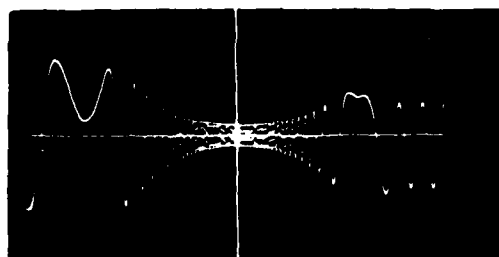
|←—50 ms—→|

|←—13 ms—→|

|←—1 ms—→|

Time

Fig. 1. Three photographs of the interferometer signal as recorded during
a typical pulse experiment in which iron is rapidly heated through
the $\alpha \rightarrow \gamma$ transformation. The horizontal scale of the signal is
expanded by factors of 1, 4 and 64 in the upper, middle and lower
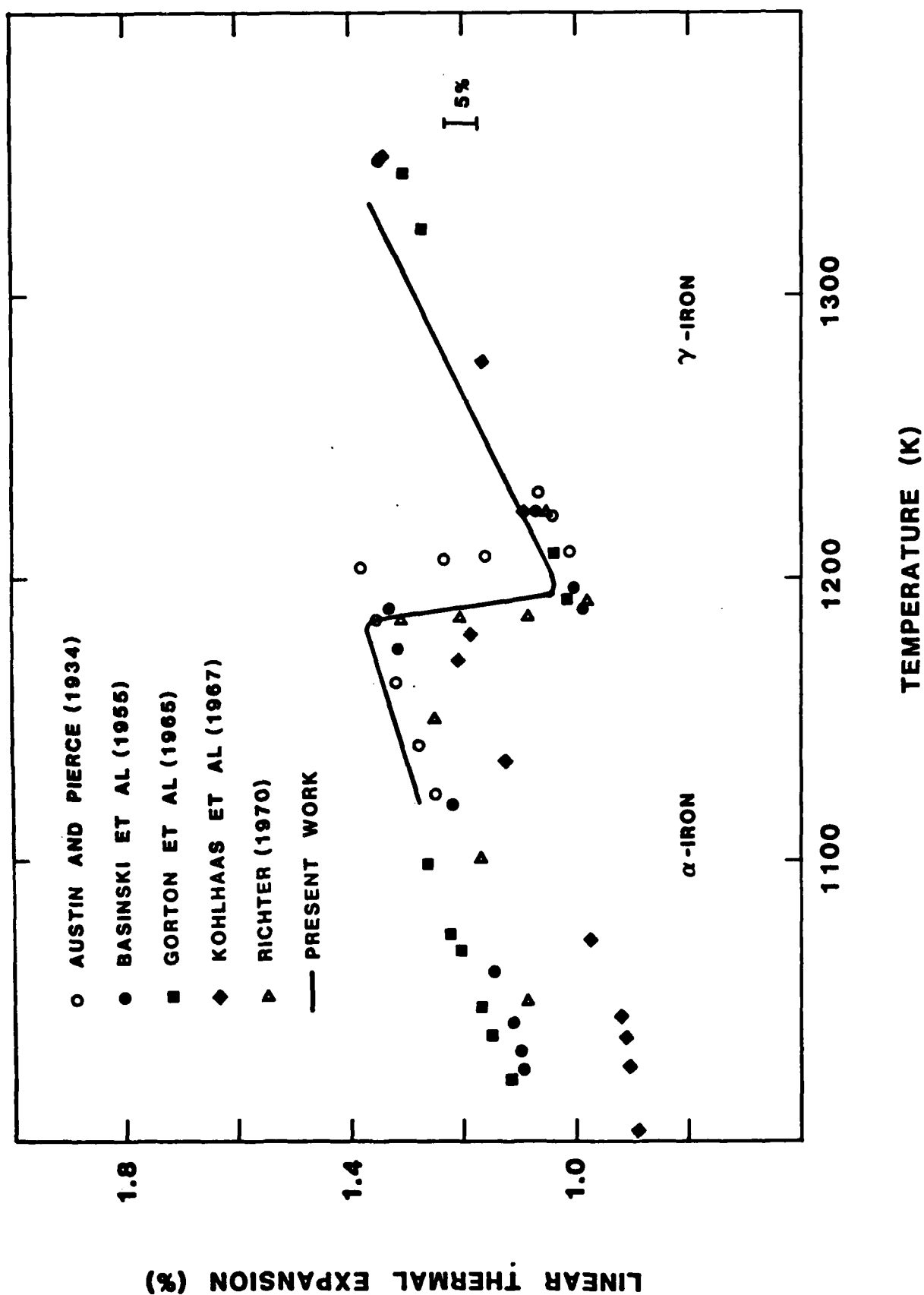photographs.

Fig. 2. Linear thermal expansion of iron in the vicinity of the $\alpha \rightarrow \gamma$ transformation: present work and data reported in the literature.

4. Heat Capacity of α- and β-Si$_3$N$_4$ in the Temperature Range 273-1173K

D. Ditmars

ABSTRACT

The relative enthalpy of α- and β-Si$_3$N$_4$ has been measured in a precision Bunsen ice calorimeter. Results are given in the form of equations and graphical data.

Silicon nitride is a refractory material of high strength and hardness, low thermal expansion coefficient, with good resistence to oxidation as well as to reaction with molten metals and slags. This material has been employed both in its pure form and as a major component of ceramic composites in high-temperature structural applications. Due to its high chemical stability in aggressive high-temperature environments, it has found application in power-generating gas turbines, permitting gas inlet temperatures as high as 1400 °C, and as a dome material in some missile and reentry applications.

Reliable high-temperature thermodynamic functions for Si$_3$N$_4$ are needed in order to calculate high-temperature equilibria involving this material. Two closely-related structural modifications of Si$_3$N$_4$ have been identified in the literature: a low-temperature (α-) form and a high-temperature (β-) form. Both of these are based on a hexagonal unit cell and differ principally in a slightly different arrangement of the nitrogen tetrahedra which enclose each Si. The β-phase is apparently metastable at low temperatures. Reported heat-capacity measurements on Si$_3$N$_4$ [2,3] are quite limited in number and exhibit a spread of up to 30% up to 1300 K. These wide differences probably have their origin in an uncertain combination of impure sample material and systematic measurement error. Apparently, none of the studies included a careful structural characterization of the sample material.

As part of an attempt to provide more accurate thermodynamic functions for Si$_3$N$_4$, we have measured the relative enthalpy of essentially pure α- and β-Si$_3$N$_4$ in a precision Bunsen ice calorimeter [1] from 273 to 1173 K. The results for β-Si$_3$N$_4$ were obtained in a prior reporting period and are now presented together with the recent results for α-Si$_3$N$_4$.

Both samples were obtained as -325 mesh powders with weight percent compositions given by the supplier's or NBS analyses as follows:

	SAMPLE "A"	SAMPLE "B"
X-RAY ANALYSIS	95% α-Si_3N_4	95-99% β-Si_3N_4
	Balance, β	< 5%, α

Spectrographic Analysis:		
N	38.25	39.40
C	0.09	*
O	1.43	*
Si_{total}	*	60.00
Si_{free}	< 0.2	*
Al	0.05	0.10
Ca	0.02	0.05
Fe	0.03	0.03
K	0.03	< 0.02
Na	0.03	< 0.02

*Not available

The analyses are consistent with 98[+] percent purity for both samples. The samples were encapsulated in hermetically-sealed Pt-10Rh alloy containers. The enthalpy of the containers-with-sample relative to their enthalpy at 273.15 K was measured at approximately 100 K intervals from room temperature to 1173 K. Enthalpy measurements on an identical empty container were available from a previous study [4].

Both sets of data were examined for outlying measurements (three for Sample "A", two for Sample "B", which were assigned zero weight) and the remaining data were fit with equations of the form

$$H_t - H_{0°c} = At^3 + Bt^2 + Ct + D(t/T) \text{ J/mole,}$$

where

H = enthalpy

t = Celsius temperature

T = Kelvin temperature.

The·coefficients and standard deviations of the fits are given below:

	SAMPLE "A"	SAMPLE "B"
A	−0.1087663 E-4	−0.1727858E-4
B	+0.3276462E-1	+0.4637328E-1
C	+0.1384411E+3	+0.1295339E+3
D	−0.1558073E+5	−0.1324359E+5

$$\sigma = 116 \text{ J mol}^{-1} \qquad \sigma = 61 \text{ J mol}^{-1}$$

Figure 1 gives the absolute and percent residuals of the fit to the
enthalpy data for Sample "A". Figure 2 gives the absolute and percent
residuals of the fit to the enthalpy data for Sample "B". Figure 4 shows
the two enthalpy functions and Figure 3 gives the difference between them as a
function of temperature. The difference appears to be significant in the
400 °C region as it exceeds the combined standard deviation of both fits.
A detailed comparison of the present data with available literature data
is in progress.

References

[1] Douglas, T. B., and King, E.G., High-Temperature Drop Calorimetry, Chapter 8 in Experimental Thermodynamics, Volume I, Calorimetry of Non-Reacting Systems, p. 293, J. P. McCullough and D. W. Scott, Eds. (Butterworths, London, 1968). See also NBS Special Publication No. 300, vol. 6, p. 181 (1970).

[2] Touloukian, Y. S., and Buyco, E. H., Specific Heat: Non-Metallic Solids, in Thermophysical Properties of Matter, The TPRC Data Series, Touloukian, Y. S., and Ho, C. Y. (Eds.), IFI, Plenum, New York (1970).

[3] JANAF Thermochemical Tables 2nd edition, NSRDS-NBS 37, June 1971, for sale by Superintendent of Documents, Washington, DC.

[4] Ditmars, D. A., and Douglas, T. B., J. Res. Nat. Bur. Stand. (U.S.), 75A (Phys. and Chem.), No. 5, 401 (Sept.-Oct. 1971).
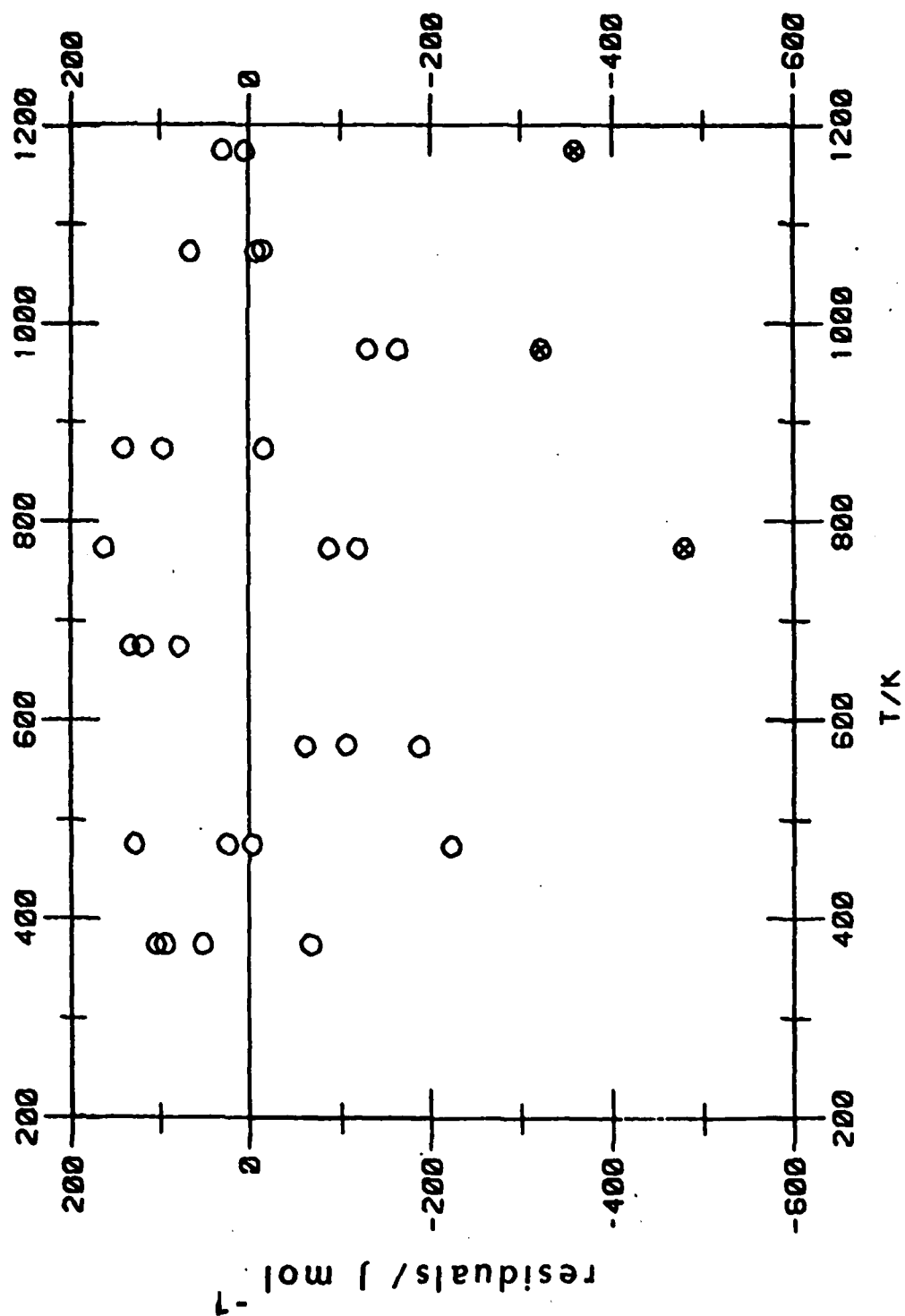
Fig. 1a. Deviation of measured relative enthalpy data for α-Si$_3$N$_4$ from least squares fit. ⊗: assigned zero weight.
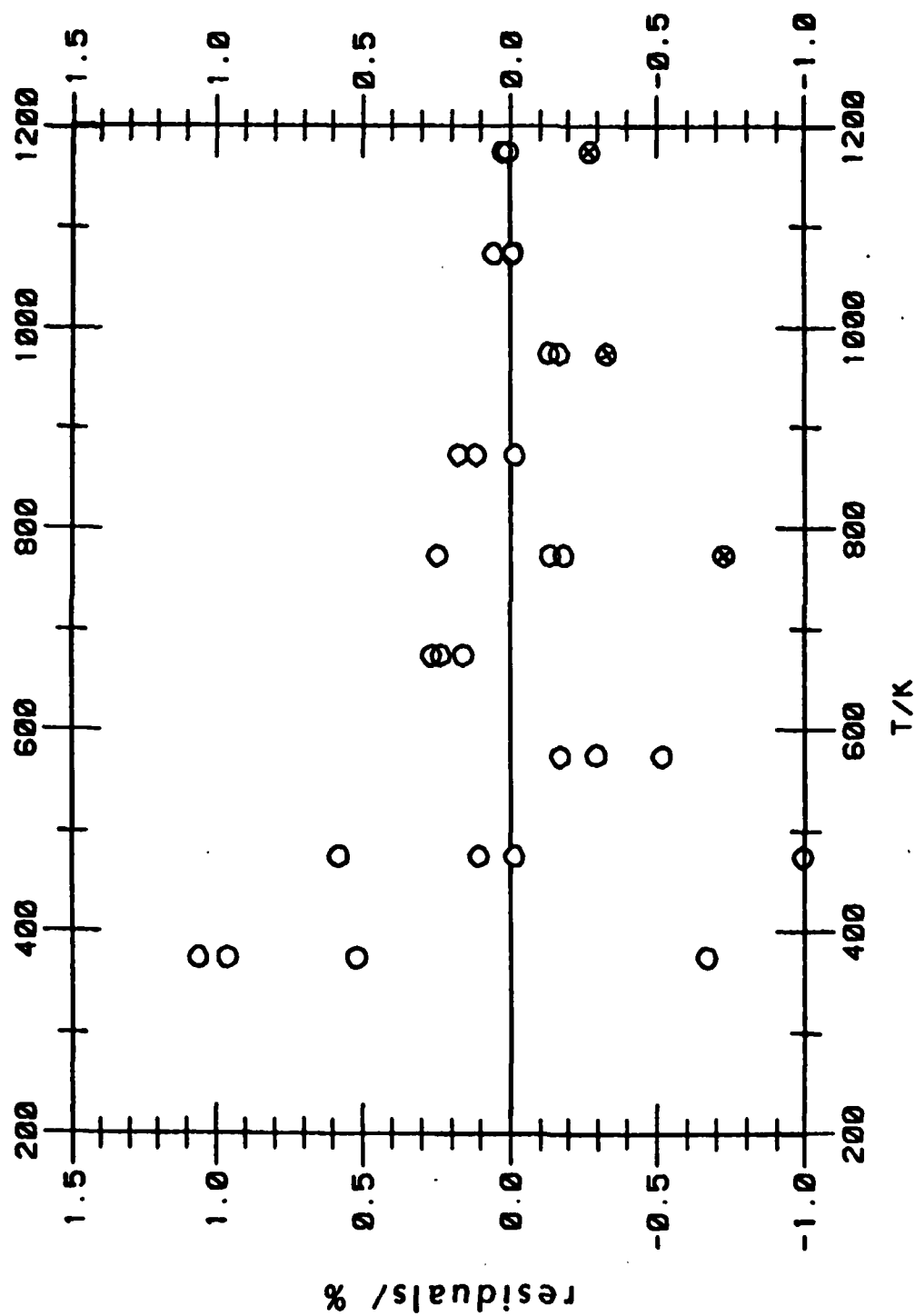
Fig. 1b. Percentage deviation of measured relative enthalpy data for α-Si_3N_4 from least squares fit.

Fig. 2a. Deviation of measured relative enthalpy data for β-Si₃N₄ from least squares fit. ⊗: assigned zero weight.

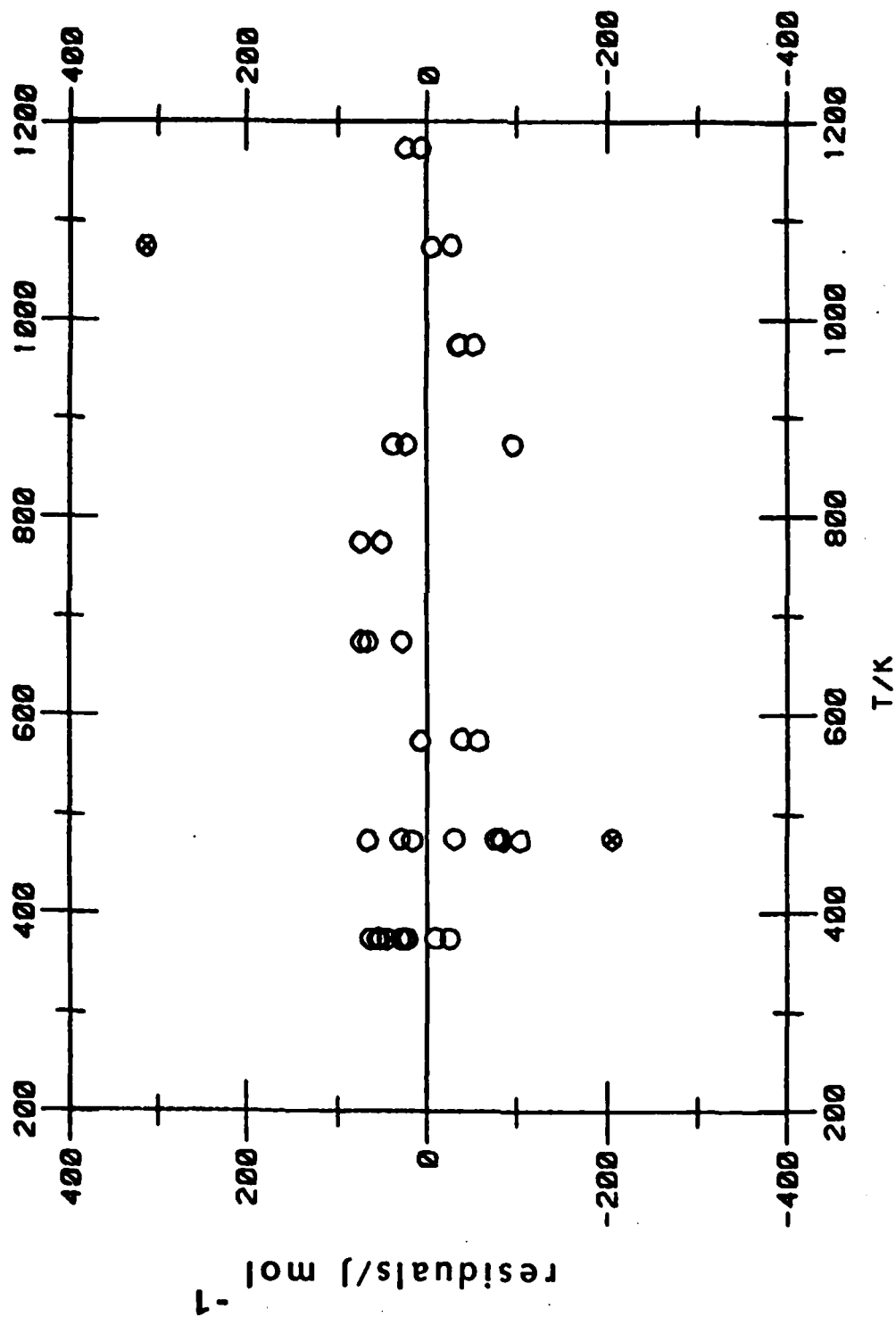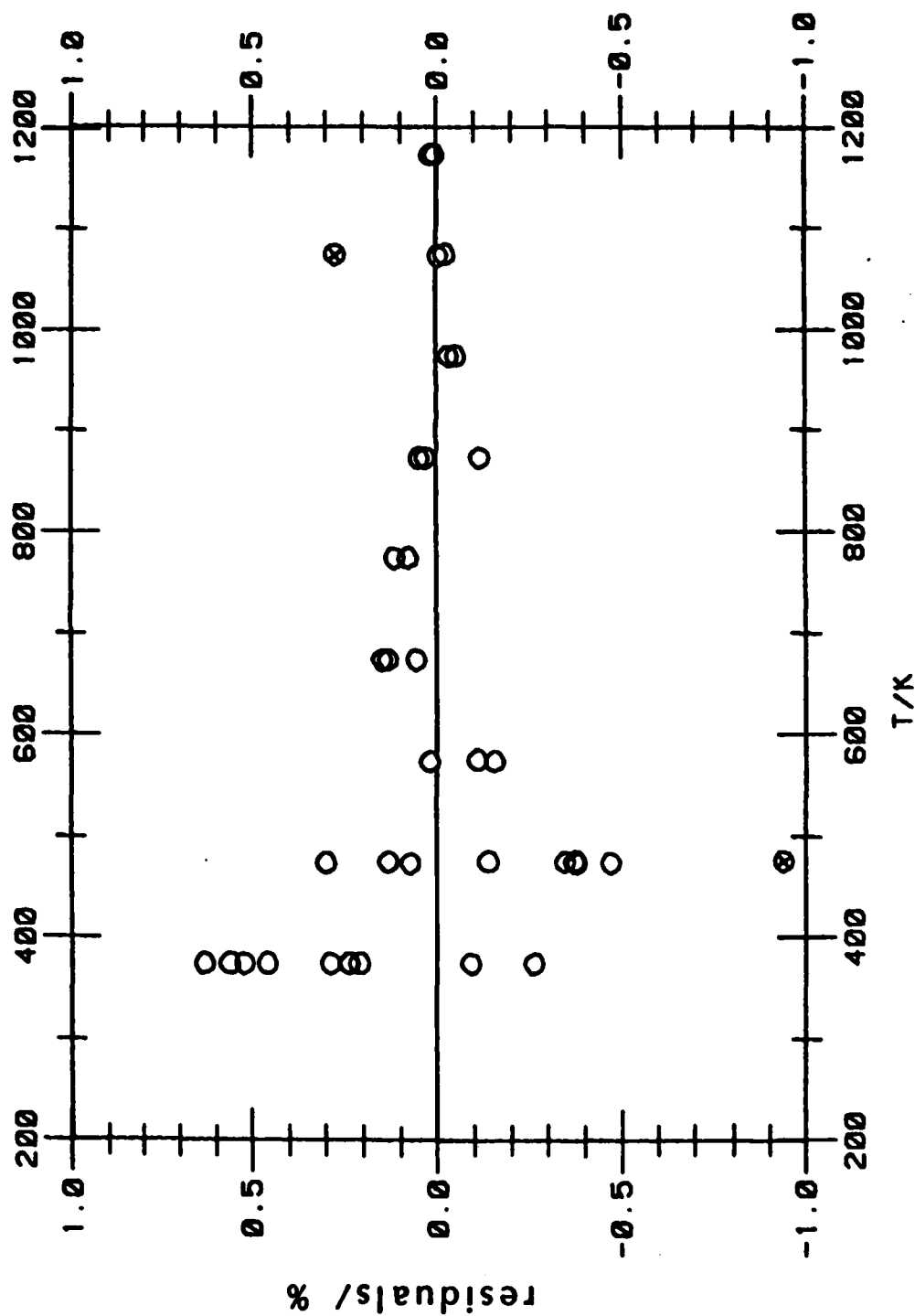Fig. 2b. Percentage deviation of measured relative enthalpy data for β-Si₃N₄ from least squares fit.

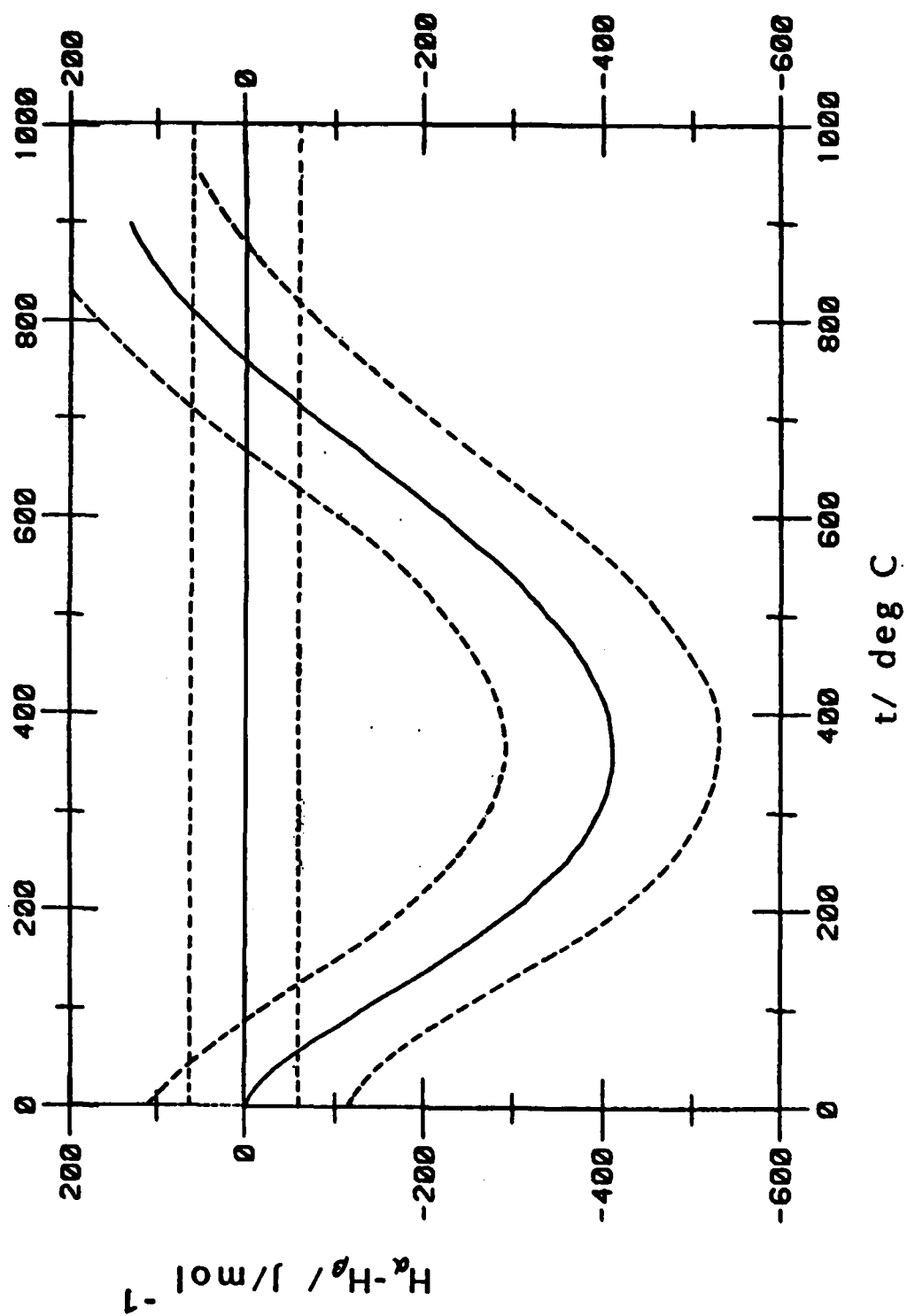Fig 3. Deviation of smoothed α-Si$_3$N$_4$ enthalpy equation (solid curve) from smoothed β-Si$_3$N$_4$ equation (base line). ---: 1σ limits.
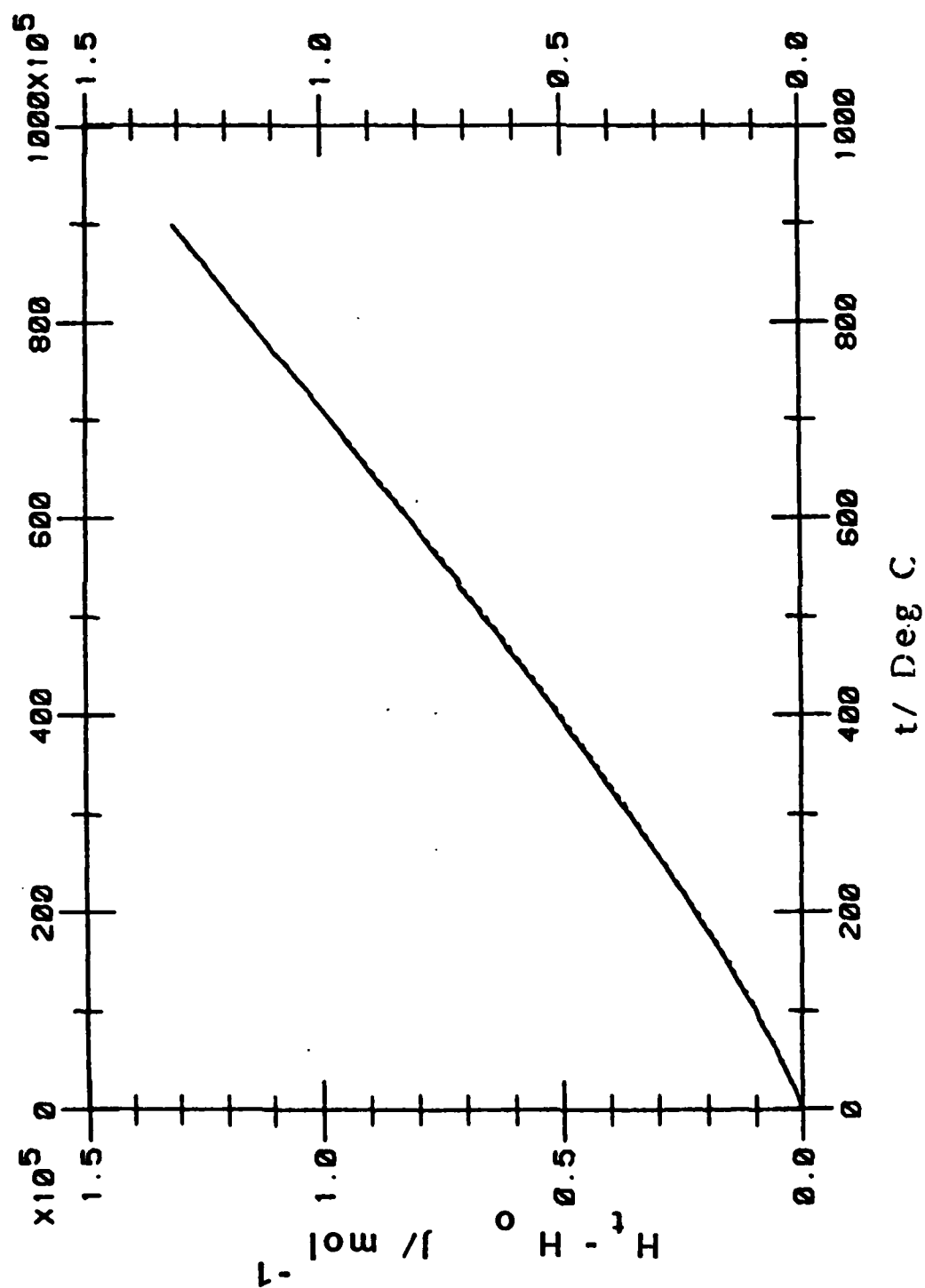
Fig. 4. Relative enthalpy functions for α-Si$_3$N$_4$ and β-Si$_3$N$_4$. (Coincident on scale shown.)

5. Critique of Calculated Thermodynamic Functions Evaluated at High Temperatures

Paul S. Julienne and Frederick H. Mies

THE THERMODYNAMIC EFFECTS OF INELASTIC COLLISIONS

ABSTRACT

Using formal scattering theory to characterize the continuum wavefunctions associated with molecular fragmentation we derive rigorous expressions for the molecular partition function Q. In particular the analysis includes the effect of inelastic collisions which are introduced by the off-diagonal elements of the scattering matrix $\underline{S}(E)$ at each total energy. Expressions are reduced to a simple form using the eigenphases of the associated $\underline{Y}(E)$ matrix derived from our recent multichannel quantum defect analysis (MCQDA) of molecular dissociation. The partition function $Q = Q_{el} + Q_{inel}$ can be separated into distinct elastic Q_{el} and inelastic Q_{inel} contributions. In addition rigorous interpretations of the thermodynamic effects of predissociation are derived and shown to have negligible consequences on equilibrium properties.

I. Background of Current Research

The accurate evaluation of thermodynamic properties at elevated temperatures requires proper analysis of the dissociated states of molecules. These continuum states make substantial contributions to the molecular partition functions and result in significant modifications of the equation of states and equilibrium constants for high temperature gases. Conventional spectroscopic analysis of the partition functions, as employed in the JANAF Tables, generally tend to overestimate the density of states for diatomic molecules at high energies, and therefore underestimate the degree of dissociation into atomic fragments. Alternately, explicit summations which exclude energy states which lie above the diatom dissociation limit will exaggerate the extent of dissociation. For polyatomic molecules the trends are not at all clear. Certainly the spectroscopic analysis employed in the JANAF Tables will fail at much lower temperatures. However we can not be sure whether the errors place an upper or lower bound on the molecular dissociation equilibrium constants.

Rigorous analysis of the molecular partition function can only be derived from the quantum mechanical treatment of the continuum states using molecular scattering theory. These continua are synonymous with the scattering wave-functions which define the elastic and inelastic collisions experienced by the departing fragments. This approach yields unambiguous interpretations of meta-stable, or predissociating states, as well as proper descriptions of second virial coefficients and imperfect gas effects at high temperatures. Great cal-culational simplifications can be achieved using classical phase integrals, but such techniques must first be certified by comparison to rigorous quantum results.

We have previously studied the alkali dimers [1] where the thermodynamic properties of the continuum states are dominated by the purely <u>elastic</u> scattering associated with a specific set of diatomic electronic states $|i>$. Each state of the diatom AB(i) defines an interatomic potential $V_i(R)$ which asymptotically correlates with a particular pair of atoms with internal energy $E_A(i) + E_B(i)$, i.e.,

$$V_i(R) \underset{R \to \infty}{\sim} E_i^\infty \equiv E_A(i) + E_B(i) \tag{1}$$

In the absence of any significant inelastic scattering between various electronic states, or channels as they are referred to in scattering theory, the exact quantum mechanical expression for the partition function is given as an independent summation over i,

$$Q = \sum_{i=1}^{N_T} \sum_{J=0}^{\infty} (2J+1) \left\{ \sum_{n=0}^{n^*} e^{-E_{i,n}^J/kT} + \int_{E_i^\infty}^{\infty} dE e^{-E/kT} \frac{\partial \xi_i^J(E)}{\pi \partial E} \right\} \tag{2}$$

For each total angular momentum state of the rotating molecule J the potential V_i may support a <u>finite</u> set $(n^* + 1)$ of truly bound vibrational states with eigen values $E_{i,n}^J < E_i^\infty$. It is convenient to define a bound state phase $v_i^J(E)$ for each potential [2]. This phase is defined to be a continuous function of the energy such that modular-π values coincide with the exact vibrational eigenvalues, i.e.,

$$v_i^J (E_{i,n}^J) = n\pi \tag{3}$$

At sufficiently high temperatures it is permissible to replace the summation over vibrational levels by the integral

$$\sum_{n=0}^{n} e^{-E_{i,n}^{J}/PkT} \approx \int_{0}^{E_{i}^{\infty}} dE \; e^{-E/kT} \frac{\partial v_{i}^{J}(E)}{\pi \partial E} \qquad (4)$$

and Eq. (2) can then be transformed into the <u>equivalent</u> classical expression

$$Q = (\frac{\mu 2\pi kT}{h^2})^{3/2} \; 2\pi \sum_{i} \int_{0}^{\infty} (1-e^{-V_{i}(R)/kT})R^2 dR.$$

A large reduced mass μ for the diatom helps insure a high density of vibrational levels, as given by $\partial v_{i}^{J}/\pi \partial E$, and thus justifies the condition;

$$kT \frac{\partial v_{i}^{J}}{\pi \partial E} >> 1, \qquad (6)$$

needed to obtain Eq. (5).

Above the dissociation limit in Eq. (2) there are an infinite set of continuum states which are a continuous function of the total energy $E > E_{i}^{\infty}$. Each continuum state is characterized by an elastic scattering phase shift $\xi_{i}^{J}(E)$ and the energy gradient of this quantity defines the density of continuum states which contribute to the partition function. Examples of both the bound state phase $v(E)$ and the elastic scattering phase $\xi(E)$ near a dissociation limit are shown in Figure 1. These are easily obtained for any given inter-action potential and allow for unequivocal evaluation of diatomic partition functions in the absence of any inelastic scattering.

II. Advancements in FY1983

An implicit assumption in all thermodynamic calculations has been that inelastic scattering and energy transfer processes do not contribute to high temperature equilibrium properties! Our efforts this year have been devoted to developing rigorous quantum mechanical descriptions of dissociating molecular states and deriving the exact thermodynamic expressions for the partition functions in the absence of coupling between channel states.

For a given total angular momentum J and given total energy E we can express the continuum wavefunction as follows

$$\psi_{j}^{J} = \sum_{i=1}^{N_{T}} |i, J> F_{i,j}^{J}(E,R)/R \qquad (7)$$

If the close-coupled scattering equations are solved numerically the only limitation on the accuracy of the wavefunctions is the number of electronic states N_T we choose to include in the expansion. These electronic wavefunctions $|i>$ are combined with appropriate rotational functions to construct the set of electronic-rotational channel states $|i,J>$ in Eq. (7). Since J is rigorously conserved even in the presence of inelastic scattering we will suppress this superfluous index in the following discussions. The interaction between channel states is defined by an interaction matrix.

$$W_{i\ j}\ (R)\ \underset{R \to \infty}{\sim}\ E_i^\infty\ \delta_{i,j}. \tag{8}$$

The result in Eq. (2) has been derived assuming that each radial function in Eq. (7) is diagonal and only exhibits appropriate elastic scattering boundary conditions, i.e.,

$$F_{ij}(E,\ \eta) = f_i(E,R)\ \delta_{i,j}\ \underset{R \to \infty}{\sim}\ k_i^{-1/2}\ \sin(k_i R + \xi_i) \tag{9}$$

This is justified if we equate $V_i \equiv W_{ii}$ and assume that all off-diagonal interactions in Eq. (8) are negligible. Using box-normalization of the continua at $R = R^*$ as R^* approaches infinity we can derive the exact continuum contributions to Eq. (2).

$$Q_i(C) \equiv \int_{E_i^\infty}^\infty dE\ e^{-E/kT}\ [\ \frac{\partial(kR^* + \xi_i)}{\pi \partial E} - \frac{\partial(kR^*)}{\pi \partial E}] = \int_{\xi_i^\infty}^\infty dE e^{-E/kT}\ \frac{\partial \xi_i}{\pi \partial E} \tag{10}$$

Our latest research [2] has shown that the exact form of Eq. (9) in the presence of coupling can be structured as follows,

$$F_{ij}(E,R)\ \underset{R \to \infty}{\sim}\ f_i(E,\eta)\ \delta_{i,j} + g_i(E,R)\ Y_{ij}\ (E) \tag{11}$$

where $g_i(E,R)$ is the irregular radical function which compliments f_i in Eq. (9),

$$g_i(E,R)\ \underset{R \to \infty}{\sim}\ k_i^{-1/2}\ \cos\ (k_i R + \xi_i). \tag{12}$$

In general we can show that the real, symmetric matrix $\underline{Y}(E)$ is analytic in E and can be continued across dissociation thresholds [3]. The complete expression for the partition function can be derived by boxnormalizing Eq. (11). This is accomplished by diagonalizing the matrix,

$$[\overset{\circ}{\tan}(kR^* + \xi) + Y(E)] = U[\overset{\circ}{\tan}(kR^* + \xi + \lambda)]\tilde{U}, \tag{13}$$

where $\tilde{U}U = \overset{\circ}{1}$ and the superscript '$\circ$' denotes diagonal matrices, such as $\overset{\circ}{\tan}(kR^* + \xi) \equiv \{\tan(k_i R^* + \xi_i)\,\delta_{i,j}\}$. We then obtain an expression comparable to Eq. (10), but with $\lambda_i(E)$ added to the elastic scattering phase shift $\xi_i(E)$, i.e.

$$Q(C) = \sum_i Q_i(C) = \sum_{i=1}^{N_T} \int_{E_i^\infty}^\infty dE\, e^{-E/kT}\, \frac{\partial}{\pi\partial E}\, \{\xi_i(E) + \lambda_i(E)\} \tag{14}$$

The dimensionality of the Y matrix in Eq. (11) is $(N_T \times N_T)$ and determined by the number of channel states included in Eq. (7). For a simple two state case, with E not close to either threshold E_1^∞ or E_2^∞ we derive

$$\sum_{i=1,2} \lambda_i(E) = \tan^{-1}\left\{\frac{Y_{11} + Y_{22}}{1 + Y_{12}^2 - Y_{11}^2 - Y_{22}^2}\right\} \tag{15}$$

We have performed a variety of two state calculations [4] and have found Y (E) to be a very insensitive function of E. Our most sensitive results are shown in Figure 2 where Y exhibits periodic oscillations over ranges of energy encompassing say 2000 cm^{-1}. Further, we invariably find, to high precision, that

$$Y_{11}(E) + Y_{22}(E) \overset{\sim}{=} 0 \tag{16}$$

Thus the effect of inelastic scattering appears to be totally negligible well within the continua, at least for two state couplings.

Equation (13) was derived assuming all channels are open, with $E > E_i^\infty$ for all $i = 1, N_T$. However the boundary conditions imposed by Eq. (13) must only be applied to the sub-set of open channels N_o which contribute to $N_T = N_o + N_c$ at any given E. If we block the Y matrix into an open $Y_{oo}(N_o \times N_o)$, closed $Y_{cc}(N_c \times N_c)$ and interacting $Y_{oc}(N_o \times N_c)$, $Y_{co}(N_c \times N_o)$ sub-matrices we must replace Y(E) with $Y_{oo}^T(E)$ in Eq. (13)

$$Y_{oo}^T(E) = Y_{oo}(E) - Y_{oc}[\overset{\circ}{\tan}\nu_{cc} + Y_{cc}]^{-1} Y_{co}. \tag{17}$$

Each of the N_c closed channels with $E < E_i^\infty$ contributes a bound state phase $\nu_i(E)$ to the diagonal matrix $\tan \nu_{cc} = \{\tan\nu_i \delta_{i,j}\}$ in Eq. (17). The zero-order positions of the vibrational levels $E_{i,n}$ defined by $\nu_i(E_{i,n}) = n\pi$ in Eq. (3) locate the approximate positions of the _predissociating_ levels which lie imbedded in the set of N_o open continuum channels. In the special two channel case, with channel $i = 1$ open, and channel $i = 2$ closed we obtain a single $\lambda_1(E)$ quantity in Eq. (14) for $E_1^\infty < E < E_2^\infty$ with

$$\lambda_1(E) = \tan^{-1}\left\{Y_{11} - \frac{Y_{12}Y_{21}}{\tan\nu_2(E) + Y_{22}}\right\} \tag{18}$$

This closely resembles the effect of rotational predissociation of metastable vibrational levels which lie behind rotational barriers in the simple one-channel elastic scattering case [1]. However in the present case the predissociation is due to the _inelastic_ coupling between distinct electronic-rotational state. If we can make the reasonable assumption

$$\frac{\partial \nu_2}{\pi \partial E} \gg \frac{\partial Y}{\partial \pi E} \tag{19}$$

we can integrate Eq. (14) over a narrow range of energy in the vicinity of each resonance to obtain

$$\int_{E_1^\infty}^{E_2^\infty} dE\, e^{-E/kT}\, \frac{\partial \lambda_1(E)}{\pi \partial E} \approx \sum_n e^{-E_{2,n}/kT} \tag{20}$$

and we can treat the predissociating levels associated with potential V_2 as though they were pure, stationary bound states.

From our present studies [4] we would have to conclude that the neglect of inelastic coupling in the calculation of thermodynamic functions is entirely reasonable. There are a number of subtleties associated with thresholds that could modify the partition functions, but these effects would probably be of limited importance, especially at elevated temperatures.

The biggest limitation on the general validity of our conclusion is that all our numerical evaluations were devoted to simple two-channel

couplings. It is possible that there are some fortuitous cancellations, as in Eq. (16), that are not present in the more general cases, and it remains for us to explore more complicated inelastic events.

References

[1] F.H. Mies, and P. S. Julienne, J. Chem. Phys. $\underline{77}$, 6162 (1982).

[2] F.H. Mies, J. Chem. Phys. $\underline{80}$, --- (Apr. 1984).

[3] At threshold the Y matrix must be replaced with a well characterized K matrix which is easily related to Y. This substitution is only required within about 100 cm^{-1} of threshold and will hardly effect any high temperature thermodynamic behavior.

[4] F. H. Mies and P. S. Julienne, J. Chem. Phys. $\underline{80}$, --- (Apr. 1984).

23 — $n^* + 1$

22 — n^*

21 — $n^* - 1$

$\dfrac{\nu_1(\epsilon)}{\pi}$

20 —

19 —

18 —

17 —

16 —

15 —

14 —

22.4064 →

$\dfrac{\xi_1(\epsilon)}{\pi}$

$\left(23 - \dfrac{kR_0}{\pi}\right)$ →

BOUND   CONTINUUM

$\sqrt{-\epsilon}$ ← → $\sqrt{\epsilon}$
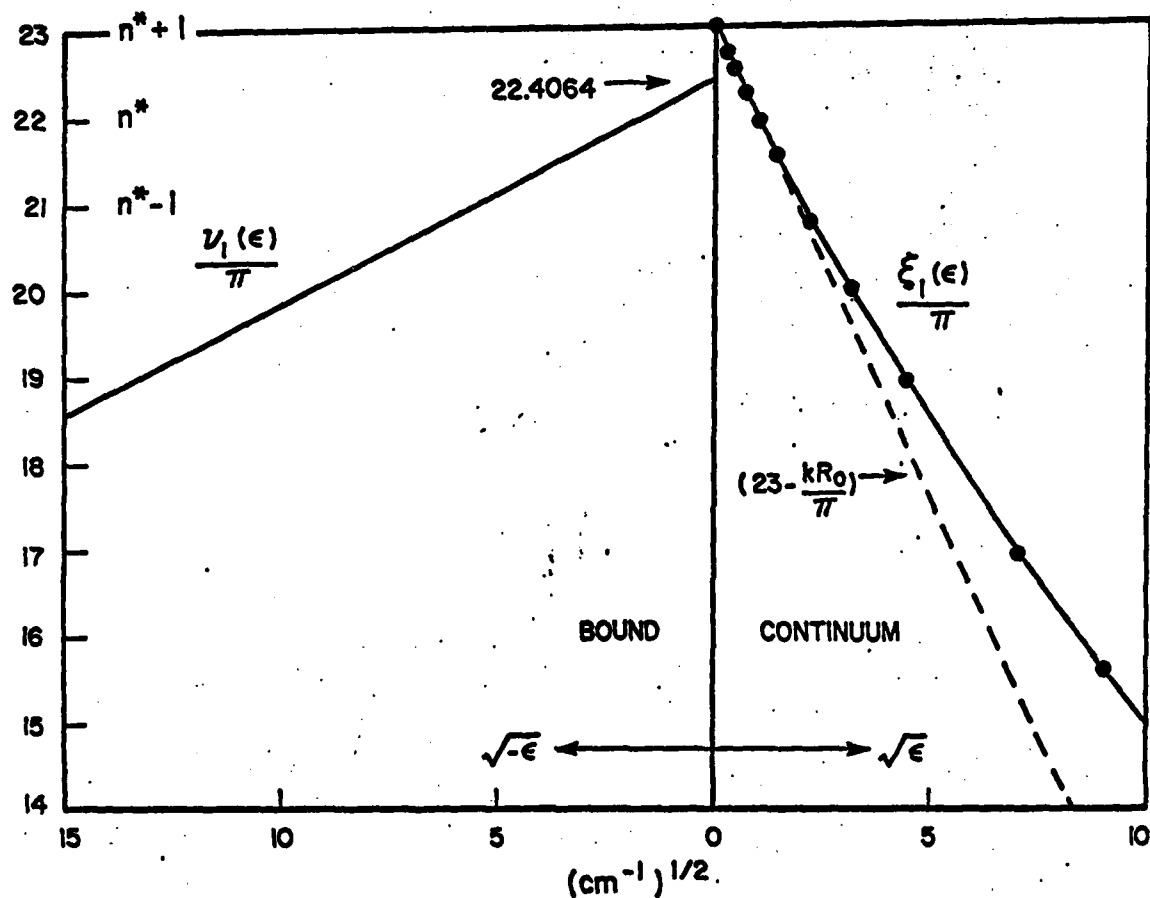
15   10   5   0   5   10

$(cm^{-1})^{1/2}$

Figure 1. Bound state $\nu_1(E)$ and elastic scattering $\xi_1(E)$ phases for a Morse potential taken to represent the $^3\Sigma_u^-$ state of O_2. A total of $(n^* + 1) = 23$ bound states exist in this attraction potential with vibrational eigenvalues $E_{1,n}$ located by the condition $\nu_1(E_{1,n}) = n\pi$, with n ranging from 0 to n^*. Levinson's theorem predicts that near threshold $\xi_1(E) = 23\pi - k_1 R_0/\pi$ for $J = 0$.
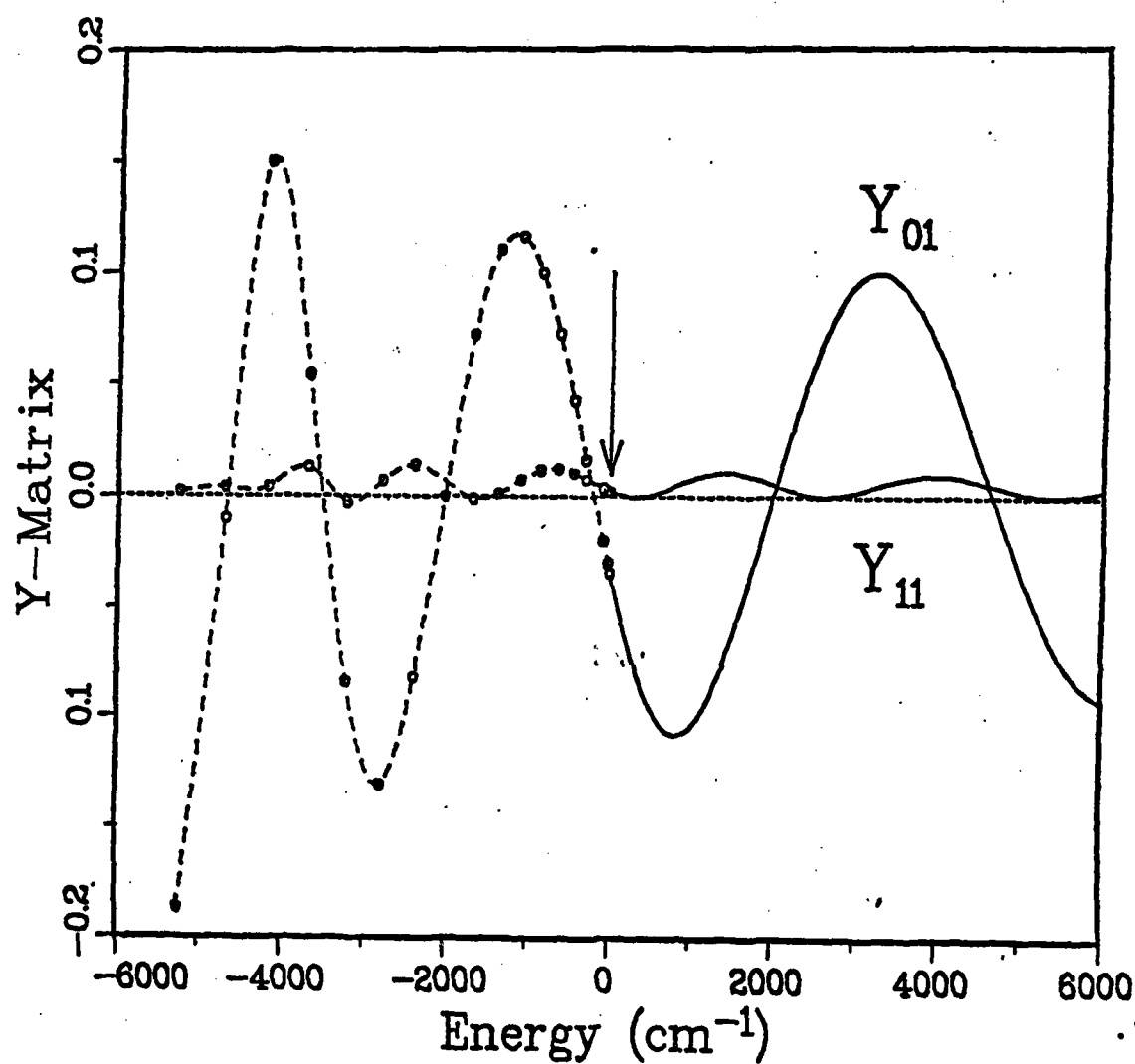
Figure 2. Examples of Y_{01} and Y_{11} matrix elements for a repulsive $i = 0$ state coupled to the attractive $i = 1$ state defined in Figure 1. The $Y_{00} \approx -Y_{11}$ values are indistinguishable on this scale and are not plotted. This appears to be a general result for two state coupling and implies that inelastic effects have a negligible effect on the thermodynamics well above threshold.

Appendix

A Multichannel Quantum Defect Analysis of Diatomic Predissociation and Inelastic Atomic Scattering[*]

Frederick H. Mies

Molecular Spectroscopy Division
National Bureau of Standards
Washington, DC 20234

ABSTRACT

Given an $N_T \times N_T$ interaction matrix $\underline{W}^\infty$ (R) which describes the dissociation of a diatomic molecule into N_T asymptotic atomic channel states, we can generate exact numerical solutions to the close-coupled scattering equations. At total energies E above the highest dissociation threshold we obtain an $N_T \times N_T$ scattering matrix $\underline{S}$ (E) which defines the asymptotic structure of the N_T-fold degenerate multichannel scattering or continuum wavefunctions. This matrix varies rapidly with energy and is non-analytic at thresholds. However, based on a multichannel quantum defect analysis (MCQDA) of the coupled equations we find that the numerical $\underline{S}$ (E) matrix can be made to yield a real, symmetric matrix $\underline{Y}$ (E) which is analytic in E. This matrix can then be analytically continued across threshold to provide rigorous analytic descriptions of the multichannel diatomic wavefunctions in the predissociating and bound-state regions of the energy spectrum.

Since the extraction of $\underline{Y}$ (E) is predicated on assigning a reference potential V_γ (R) to each channel, the detailed energy variation of $\underline{Y}$ (E) is dependent on the choice of potentials. Fortunately the physics contained in $\underline{W}^\infty$ (R) generally dictates an obvious set of reference potentials which usually make $\underline{Y}$ (E) slowly varying. As E is reduced below threshold we can use $\underline{Y}$ (E), often well represented as a constant over a wide range of energies, to provide a description of the predissociating molecule, including such observable properties as line widths, level shifts, and branching ratios. At still lower energies, when all channels are closed, $\underline{Y}$ (E) offers a complete, non-perturbative description of the configuration interaction between bound electronic-rotational states of the molecule.

Although many insights in this paper are provided by a WKB analysis of the reference solutions associated with each reference potential, the MCQDA yields a complete quantum mechanical description of the exact close-coupled wavefunctions. The quality of these wavefunctions is limited only by the accuracy of the molecular potentials and interaction matrix elements that are used to construct $\underline{W}^{\infty}(R)$, and by the number N_T and specific set of channels we choose to include in the close-coupled theory. The analysis is equally valid when applied to either adiabatic avoided crossings or diabatic curve crossings. More importantly, the formal structure of the close-coupled wavefunctions dictated by MCQDA yields a rigorous framework for the analysis of strongly interacting continuum, predissociating, and bound state channels without recourse to perturbation theory.

A Multichannel Quantum Defect Analysis of Two-State Couplings in Diatomic Molecules[*]

Frederick H. Mies and Paul S. Julienne

Molecular Spectroscopy Division

National Bureau of Standards

Washington, DC 20234

Abstract

A multichannel quantum defect analysis (MCQDA) for non-coulomb potentials is applied to two-channel coupling in diatomic molecules. Given the exact 2x2 scattering matrix $\underline{S}(E)$ obtained at a single energy above the dissociation threshold $\varepsilon > 0$, we can extract an analytic, energy-insensitive 2x2 matrix $\underline{Y}(\varepsilon)$ which can be extrapolated across thresholds and yield a complete description of predissociating molecules. The predicted widths, shifts, and lineshapes obtained from MCQDA are in quantitative agreement with the exact numerical results and confirm the remarkable simplicity that can be achieved in describing diatomic systems near dissociation limits. The analysis is equally applicable to either adiabatic avoided crossings or diabatic curve crossings. The validity of MCQDA is independent of coupling strength and can quantitatively describe strongly overlapped predissociating resonance states. The application of MCQDA to the bound state spectrum, when both channels are closed, is discussed.

6. Stability and Growth of Graphitic Layers

Principal Investigators: S. E. Stein

                            R. L. Brown

Introduction

The nature of the chemical steps and intermediates responsible for the formation and decomposition of graphitic materials are not even vaguely known. Progress in this area is seriously impeded by the lack of a reliable theory for treating reactive chemical structures in these substances, particularly those at edges and defects where chemical reactions are commonly presumed to occur.

To treat these structures within very large molecules, computationally facile, but reliable theories are required. Fortunately, such theories are available for the π-electron networks that constitute graphite. However, until recently these theories have been used almost exclusively for relatively small molecules. Applications of these theories to very large graphitic molecules and their subsequent testing and refining by experiment are the major long-term goals of this program.

Progress During FY-83

A number of theoretical approaches to chemical properties of "graphitic" structures have been examined. For estimation of resonance energy in molecules we have used the simplest form of structure-resonance theory, SRT [1], a form that relates the resonance energy of a conjugated species to the logarithm of its number of Kekulé structures. To obtain localization energies needed for prediction of reactivity we have employed a first-order perturbation treatment [2], and to obtain odd-electron densities in graphite-like free radicals and energy levels for all π-electrons we have used Hückel molecular orbital (HMO) theory.
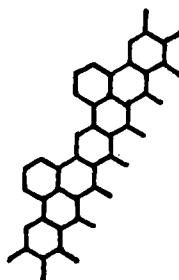
Studies have focused on a series of highly condensed benzenoid molecules. Members of a given series differed in size but had the same edge and corner construction. The following four edge structures were considered,
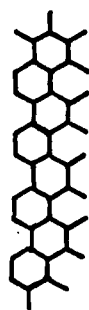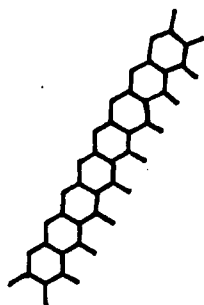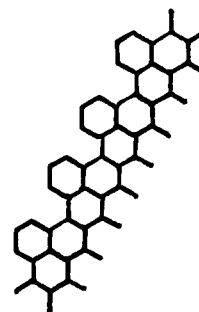

A   B   C   D

Examples of the first few members of series A and B are given in Figure 1. In general, for each edge-type a number of different corner structures are possible depending on molecular size and shape.

Stabilities of benzenoid layers for hexagonal series with edge-types A-D are shown in Figure 2 as a function of molecular size. Stabilities are represented as the logarithm of the number of Kekulé structures per π-electron ($\equiv n_\pi^{-1} \ln[\#$ Kekulé structures] where n_π is the total number of π-electrons). In the simplest form of SRT, $\ln(KSPE)$ is proportional to the resonance energy per π-electron. Molecular size is represented by $n_\pi^{-1/2}$, which is roughly proportional to the number of edge carbon atoms. This function is chosen since it was found to clearly show the behavior of $\ln(KSPE)$ as $n_\pi \to \infty$.

As shown in Figure 2, stabilities of benzenoid layers depend strongly on the nature of the edges. For each series studied, as molecular size

increases, ln(KSPE) approaches an asymptotic value. Perhaps surprisingly, different series can approach distinctly different asymptotic values. This suggests that even in arbitrarily large layers, average π-electron energies may depend on the nature of the edges. Several additional calculations using a more complex form of SRT [3] predict similar relative stabilities and asymptotic behavior.

The most stable series has edges that contain only phenanthrene-like units (edge-type A, often referred to as "arm-chair" edges). These structures represent one of the two possible ways of, in effect, cutting regular hexagonal molecules out of an infinite benzenoid sheet.

The least stable series has straight, anthracene-like edges (edge-type B, often called "zig-zag" edges) and represents the second possible way of cutting a regular hexagonal structure out of an infinite benzenoid sheet.

The finding that molecules with B-edges are less stable than molecules with A-edges is consistent with the general finding that "straight-edge" polyaromatic structures are less stable and have fewer Kekulé structures than do "bent" structures. For example, in the isomerization of anthracene to phenanthrene, $\Delta H = -6 \pm 2$ kcal mol^{-1} and the number of Kekulé structures increases from four to five.

Series C, while closely related to series B in structure, actually approaches the same asymptotic value of KSPE as does the most stable series A. This finding suggests that the relative orientation of bonds and edges, in itself, is not a factor determining resonance stability.

The stability of series D falls between that of B and C and approaches an intermediate limit for KSPE. Relative stabilities of series C and D are opposite to predictions of group additivity [4].

It appears that the stability of a benzenoid layer cannot be properly rationalized in terms of separate contributions from edge structures and interior rings. The degree of coupling (conjugation) between edge and interior atoms can be a dominant factor and is directly reflected in the present determinations of KSPE.

We now consider reactivity. Reactivity will be analyzed in terms of electron localization energies, which are energies required to isolate a π-electron from the rest of the conjugated system. Localization energies δE_π for the π-electrons are estimated by applying first-order pertubation theory to the Hückel molecular orbitals [2]. In Figure 3 are given representations of δE_π for two polyaromatic layers, one with edge-type A, the other with edge-type B. Activation energies for chemical reaction at the position of electron localization are often considered to be linearly related to δE_π, so that the smaller the δE_π value, the greater the reactivity.

In the more stable layer (A), reactivity is predicted to be quite uniform throughout the later, even at the edges, although regions of lower and higher reactivity can be seen near the edges. For the less stable layer (B), edge atoms are far more reactive than interior atoms, and edge reactivity increases toward the center of each edge. Clearly A, which is predicted to be more thermodynamically stable than B, is also far less reactive.

Additional calculations on members of series A and B show that the average of all δE_π values approaches zero as molecules increase in size. Average reactivities are therefore predicted to increase and approach one another with increasing size and, in accord with experiment, large

graphitic layers are predicted to always be highly reactive. For both molecules given in Figure 3, both the most and least reactive positions are located near the edges. In the more stable molecule (A), δE_π for these two positions are 1.41 β and 2.31 β, while for the less stable molecules (B) these values are 0.484 β and 2.28 β. For comparison, δE_π for benzene is 2.31 β and for the most reactive position in anthracene (the 9-position) the value is 1.26 β.

The present calculations yield, as byproducts of the above reactivity calculations, HMO odd-electron densities [2] (Figure 4).

Finally, we have used HMO theory to examine properties of all π-electrons in two-dimensional layers containing up to 1500 carbon atoms. This theory yields properties of each occupied orbital and can be used for examining spectroscopic and electronic properties. An example of results of these calculations is given in Figure 5 for the homologous series A.

We postpone presenting a more detailed analysis of reactivity and electron density until we have parameterized the present calculations using results of more accurate theories. This work is now in progress.

In summary, we have shown that it is practical to apply reliable theories for π-electrons in benzenoid systems to very large, well-defined graphitic planes. Initial results of these calculations show that when viewed as members of homologous series these planes can be examined in a systematic manner. The degree of coupling between edge and interior rings can be a particularly important factor whose magnitude can not always be estimated by simple comparisons to small polyaromatic molecules.

References

1. Swinborne-Sheldrake, R.; Herndon, W. C. Tetrahedron Lett. 1975, 10, 755; Herndon, W. C.; Ellzey, M. L., Jr., Amer. Chem. Soc. 1974, 96, 6631.

2. Clar, E. J., "Polycyclic Hydrocarbons", Vol. 1, Academic Press, New York, 1964, pp. 37-38.

3. Cox, J. D.: Pilcher, G., "The Thermochemistry of Organic and Organometallic Compounds", Academic Press, New York, 1970.

4. Stein, S. E.; Golden, D. M.; Benson, S. W., J. Phys. Chem. 1977, 81, 314.

Publications and Presentations

(1) "Counting of Resonance Structures for Large Benzenoid Polynuclear Hydrocarbons", J. Computational Chem., 1984.

(2) "A Chemical Theory of Graphite-Like Molecules", submitted to Carbon, 1983.

(3) "A Chemical Theory of Graphite", presented at the International Conference on Coal Science, Pittsburgh, PA, August 1983.

(4) "A Chemical Theory of Graphite", presented at the "16th International Carbon Conference", San Diego, CA, July 1983.
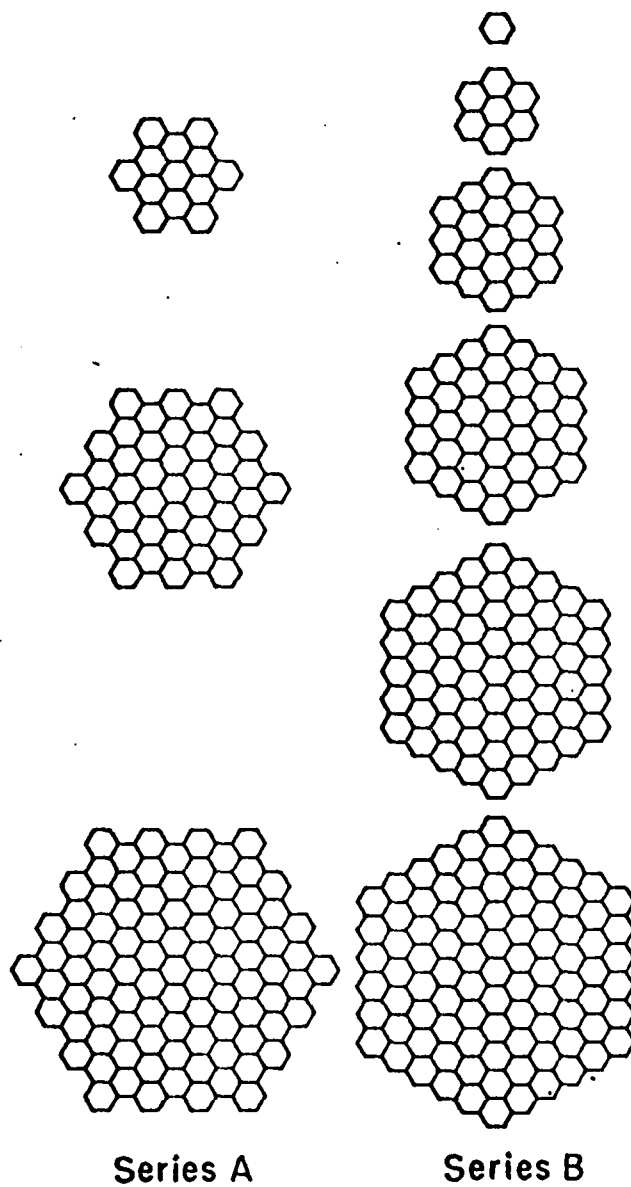
Figure 1.   Two Examples of Homologous Series Studied.
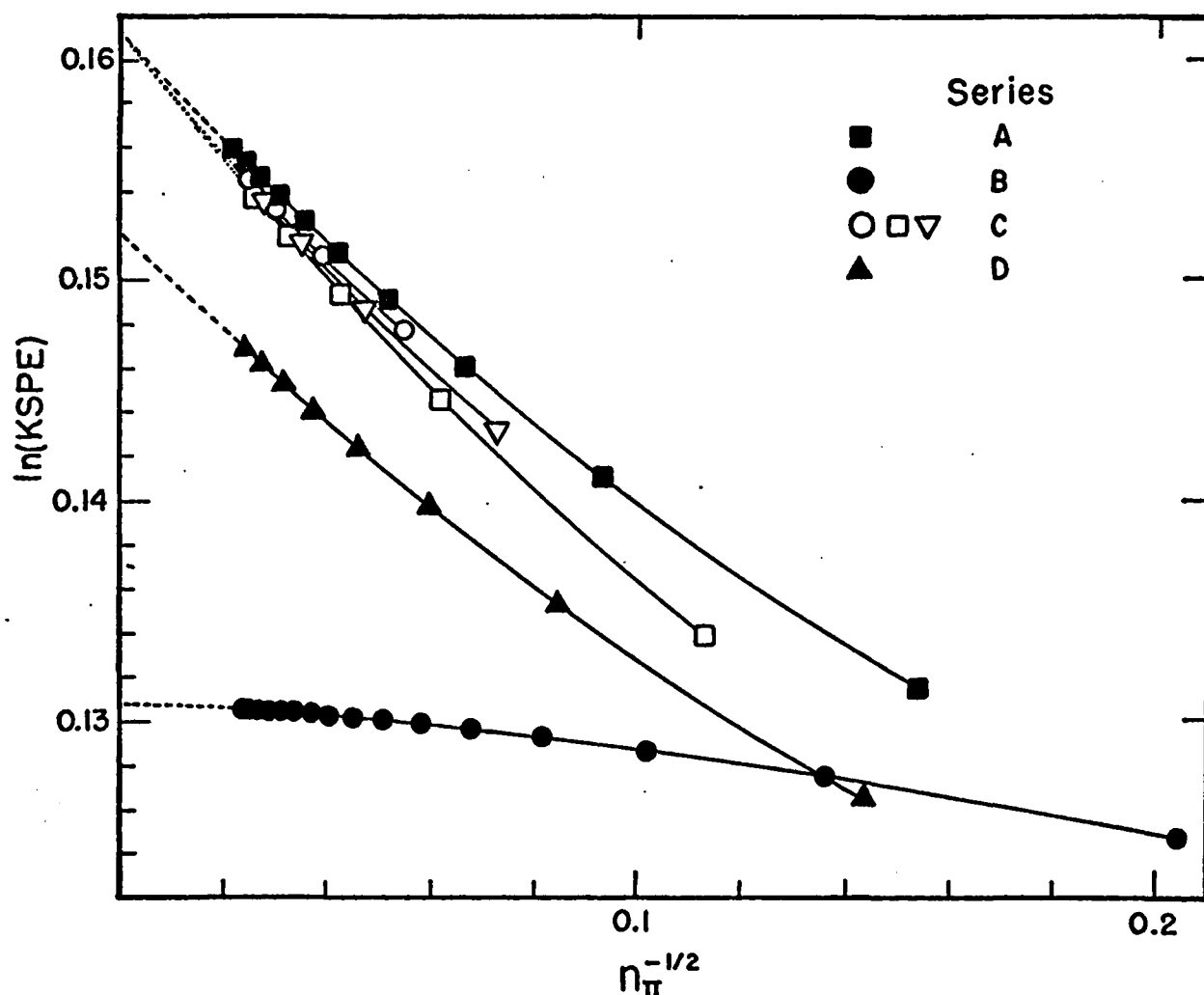
Figure 2.   Stabilities of Hexagonal Benzenoid Layers. n_π is the total number of π-electrons, KSPE is the number of Kekulé structures per π-electron (for benzene $n_\pi = 6$, the number of Kekulé structure is 2, KSPE = $2^{1/6}$ = 1.12, and ln(KSPE) = 0.116). Edge structures of series A-D are given in the text. The three series with edge C contain different corner structures (= I ; $\nabla \equiv$ II 0 = III). For other edges, only series with the most stable corner structures are shown. Intercepts at $n_\pi^{-1/2}$ = 0 were obtained by least squares analyses of the points shown.

b

a
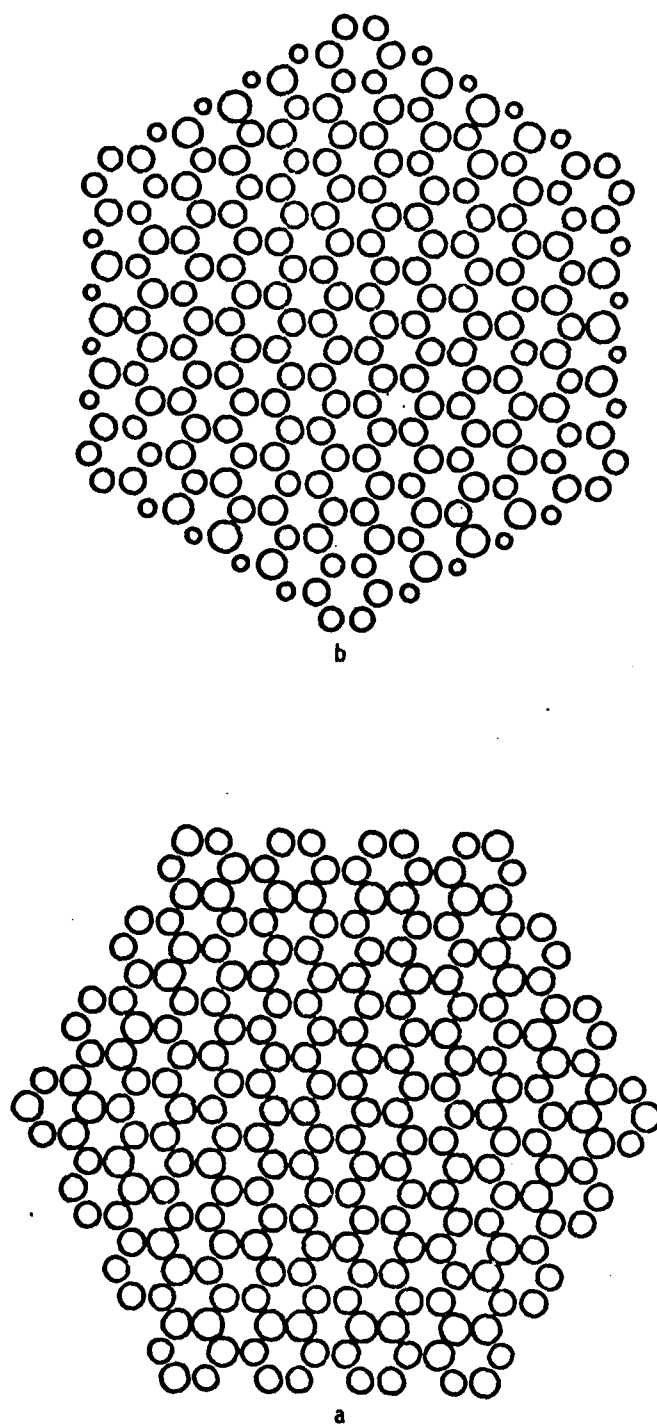
Figure 3.   PMO Location Energies. Structure A represents a member
of the most stable series (series A, n_π = 222) and structure B
represents a number of the least stable series of comparable
size (series B, n_π = 216). Areas of circles are proportional
to δE_π, hence the smaller the cricle, the greater the
reactivity.
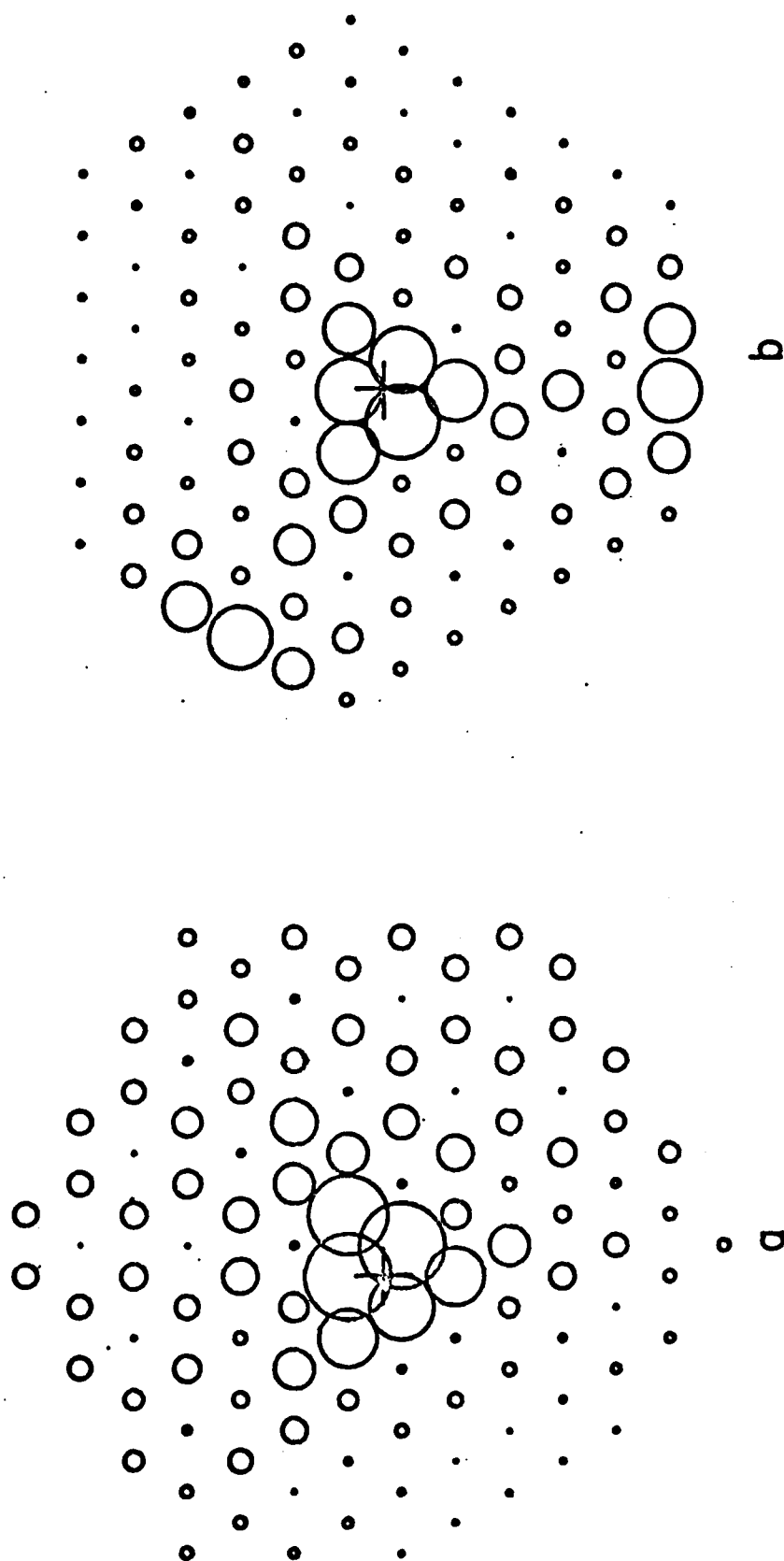
Figure 4.   HMO Electron Densities. These species are the free radicals obtained by localizing an electron in the molecules represented in Figure 3 at the position denoted by the corss. Areas of circles are proportional to HMO electron densities. Note that half of the carbon atoms in these molecules, including the position of localization, have zero HMO electron densities.

HUCKEL MÓ ENERGY LEVELS

increasing size→

Figure 5.   Occupied HMO Energy Level for members of "zig-zag" edge

series (series B, Figure 1).

BUILD-UP AND IRRADIATION OF CARBON CHAINS UNDER NEAR-VACUUM CONDITIONS

Principal Investigator: S. G. Lias
Collaborating Investigator: T. J. Buckley

(0.5 Man-Year in FY 83)

Introduction

The Spacecraft Survivability research initiative addresses the areas of generation and dispersal of smokes and obscuring materials in space, the kinetics of evaporation of refractory materials under laser irradiation, and of condensation processes in space leading to the formation of microscop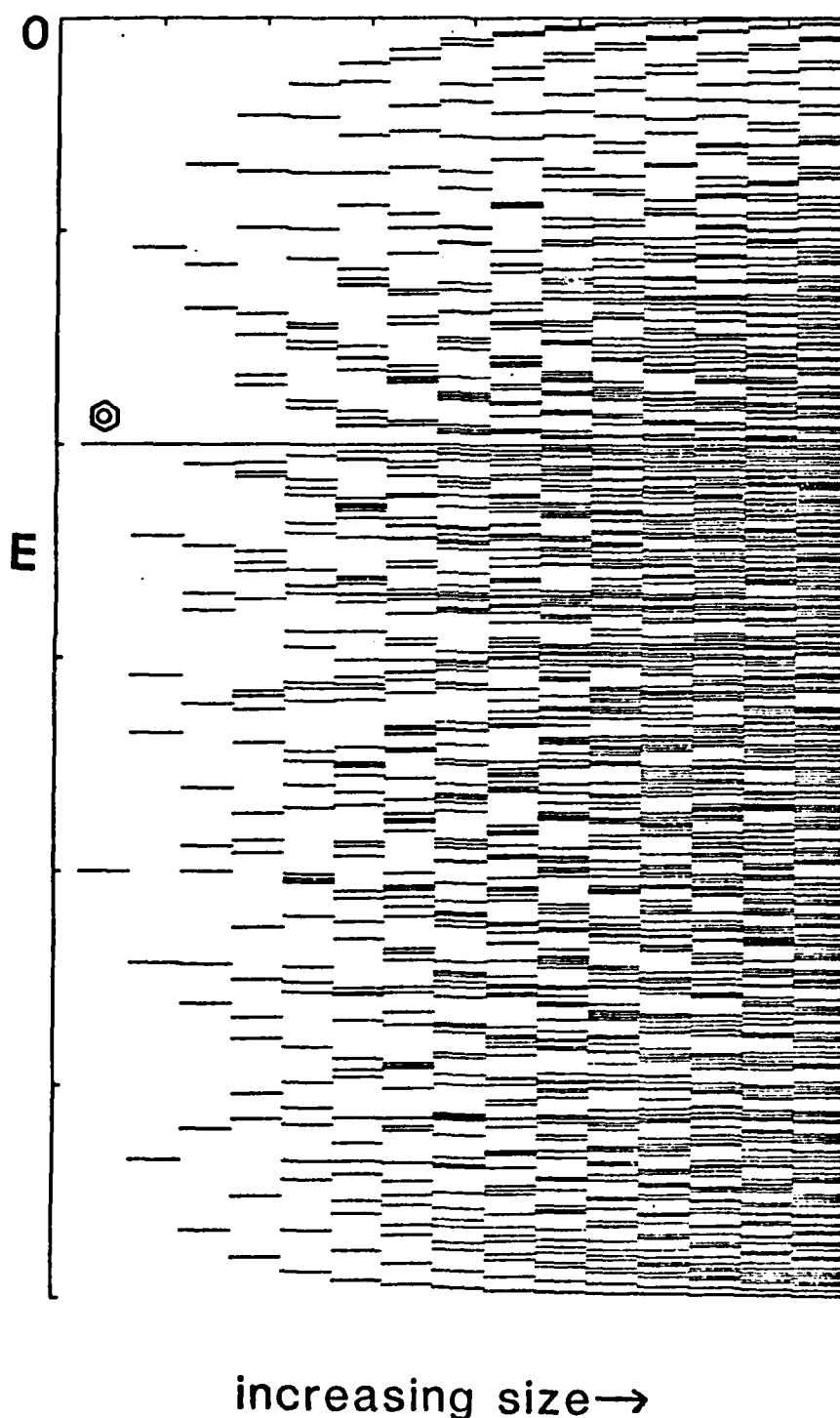ic particles. Since one possible primary constituent of a protective coating for spacecraft is carbon, this task addresses (1) the kinetics of condensation processes leading to the build-up of hydrogen-deficient carbonaceous material under near-vacuum conditions, and (2) the chemical consequences at a molecular level of the laser irradiation of such systems. In FY 84, studies are being initiated in which polyacetylenic condensation ions will be irradiated using a laser to investigate (1) their decomposition by high energy photons, and (2) the effects of a vacuum environment on the build-up mechanisms. Work will also be initiated to examine the chemistry which occurs upon irradiation of selected solid surfaces under simulated space conditions.

This project utilizes the NBS ion cyclotron resonance spectrometer for the study of gas phase ionic reaction mechanisms leading to the build-up of long polyunsaturated carbon chain ions in hydrogen-deficient systems such as diacetylene, $HCCCCH$, cyanoacetylene, $HCCCCN$, or vinylacetylene, $HCCCHCH_2$. The ion cyclotron resonance spectrometer (ICR) is an instrument in which ions are formed in a gas sample by a pulsed electron beam, and then are held in cyclotron motion for times as long as a second by the presence of a high magnetic field (~14 kilogauss). Although the pressure in the spectrometer is typically 10^{-6}

torr, the ions are trapped for times long enough that they undergo a sufficient number of collisions with neutral molecules in the system that chemical reactions with neutral molecules in the system go to completion. The ions are detected through the absorption of energy from a pulsed radiofrequency field and the abundance of an ion of a given mass can be followed as a function of time. The vacuum chamber in which the reaction cell is contained is fitted with a window for the photochemical/laser studies of photon-induced dissociation processes and/or photon excitation of the reacting ions.

Progress Report, FY 83

A. Completion of Study on Condensation Kinetics and Mechanisms

In FY 83, kinetic studies of both rate constants and reaction mechanisms leading to the formation of hydrogen-deficient carbon-chain ions systems were completed in the following systems: diacetylene, cyanoaetylene, and vinylacetylene. A manuscript describing the work is currently being prepared for submission to the Journal of Physical Chemistry. The findings of most interest to the program on Spacecraft Survivability are: (1) Ions formed in acetylenic materials will condense with the parent molecules at every collision; (2) At pressures of 0.01-0.1 torr (approximately 10^{-5} atm) the condensation product will be collisionally stabilized, and will react further with the parent molecular material with a high efficiency; successive condensations lead eventually to the formation of high molecular weight hydrogen-deficient carbon chains; (3) At pressures of 10^{-6} torr (approximately 10^{-9} atm), the condensation products will dissociate by loss of hydrogen or acetylene, but the resulting product ionic species do react further with the parent molecules to build up larger ions, although at low pressures the lengthened collision interval slows the process. A more detailed summary of the results to be reported in this paper is attached.

B.   Instrumentation Development

During FY 83, considerable effort was given to preparing the instrument for the laser irradiation experiments planned for FY 84. The system was modified in four major areas: (1) the vacuum system was improved; (2) a light source was installed; (3) the analog detection electronics were up-dated; and (4) the automation of the data acquisition and control system was improved.

(1)   A new high vacuum chamber was completed and installed. A quartz window at the end of the chamber allows UV-VIS light to enter the trapped ion cell for the photodissociation experiments. An inlet for a solids probe was added for future studies with low vapor pressure compounds. The vacuum system was also modified by the addition of a pressure tranducer to monitor the sample inlet gas pressure. An automated leak valve was installed to allow the computer to set and regulate the gas pressure in the ion cell. This eliminates slow pressure drifts which formerly distorted the ion decay signals. Modifications were also made to the bake out and temperature control system to provide more accurate temperature readings.

(2)   A pulsed tunable dye laser was obtained on loan for use in our experiments. The laser has been set up and shown to work in the 400-700 nm range. The laser has sufficient energy per pulse to photodissociate a detectable number of ions; the short pulse duration will permit one to monitor ions in the time-resolved mode.

(3)   The analog detection electronics on the capacitance bridge detector have been modified to allow more accurate adjustment of the ion signal baseline. The electron beam pulse controller has also been improved to regulate the ionization current. This modification stabilizes the number of ions generated during each pulse of the electron beam thus decreasing ion frequency fluctuations caused by varying space-charge affects.

(4)   The data acquistion hardware has been expanded to allow a greater degree of automation. These changes include a system for computer stabilization of drift in the magnetic field caused by our aging power supply. The ionization pressure gauge and capacitance manometer have been interfaced to the computer so their readings may be digitized. The ion signal intensity is now read by a digital voltmeter which is triggered by the sample and hold pulse. This improvement eliminates errors caused by droop of the sample and hold circuit. The sensitivity of the ionization gauge is now automatically determined by remote control of the leak valve, ionization gauge, and capacitance manometer. A new disk operating system was installed to increase the speed of file storage and retrieval as well as freeing memory for program development. New kinetic analysis software permits for the first time an analysis of data for an experiment still in progress. This greately improves the efficiency of operation. Figure 1 illustrates results obtained in the cyanoacetylene system using the new data acquisition system.
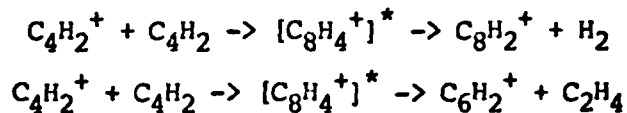
# SUCCESSIVE ION-MOLECULE CONDENSATION REACTIONS IN ACETYLENIC COMPOUNDS

by

Sharon G. Lias, L. W. Sieck, and Thomas J. Buckley

Summary of Publication in Preparation

Successive ion-molecule condensation reactions have been studied in diacetylene, cyanoacetylene, and vinylacetylene. For example, in diacetylene, the pulsed electron beam initially forms $C_4H_2^+$ ions which react with neutral diacetylene molecules through two competing channels:

$$C_4H_2^+ + C_4H_2 \rightarrow [C_8H_4^+]^* \rightarrow C_8H_2^+ + H_2$$

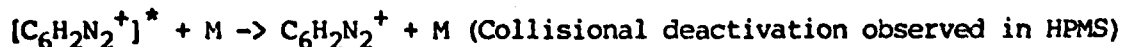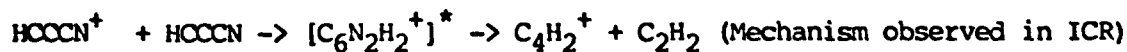$$C_4H_2^+ + C_4H_2 \rightarrow [C_8H_4^+]^* \rightarrow C_6H_2^+ + C_2H_4$$

(where the species in brackets is the excited ion formed by condensation of $C_4H_2^+$ with diacetylene). The product ions formed in these reactions then react further with diacetylene:

$$C_6H_2^+ + C_4H_2 \rightarrow C_{10}H_4^+$$

$$C_8H_2^+ + C_4H_2 \rightarrow C_{12}H_4^+$$

$$C_{12}H_4^+ + C_4H_2 \rightarrow C_{16}H_6^+$$
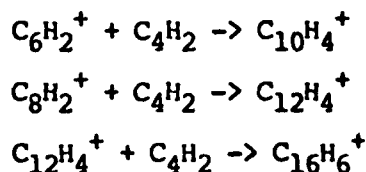
On the time scale of these experiments the $C_{16}H_6^+$ ions do not undergo enough collisions for further reaction sequences to be observable (collision interval ~2-3 msec).

In order to extend the number of collisions which the hydrogen-deficient carbon chain ions undergo, the ICR measurements were complemented by a set of experiments carried out at a 10^4-fold higher pressure (10^{-3} - 10^{-2} torr) in the NBS pulsed electron high pressure mass spectrometer.

A typical set of experimental results obtained in the pulsed ion cyclotron resonance spectrometer is shown in Figure 1, which plots the abundances of ions formed in cyanoacetylene as a function of time. Figure 2 shows the abundances of the ions formed in this compound in the high pressure instrument as a function of pressure; these results can be compared with those shown in Figure 1, where ion abundances observed at a single pressure are observed as a function of time. In both cases, in going from left to right in the Figure one is examining the effects of additional collisions of the ions with the neutral molecules which are the predominant species present in the system. The initial reaction sequence observed in the two instruments is similar, except that at "high" pressures the $[C_6N_2H_2^+]$ condensation ion formed in the initial step does not dissociate by loss of acetylene, but rather is collisionally-stabilized.

$$HCCCN^+ + HCCCN \rightarrow [C_6N_2H_2^+]^* \rightarrow C_4H_2^+ + C_2H_2 \text{ (Mechanism observed in ICR)}$$

$$[C_6H_2N_2^+]^* + M \rightarrow C_6H_2N_2^+ + M \text{ (Collisional deactivation observed in HPMS)}$$

The high pressure mass spectrometric data also show further reactions of product ions

to form product ions with as many as 21 carbon atoms; under the "high pressure" conditions, the successive condensation ions are collisionally stabilized and do not dissociate.

A summary of the experimental results in the cyanoacetylene and diacetylene systems is given in the accompanying table. In both systems, it is seen that the first step in the condensation mechanism is extremely efficient, occurring on every collision between an initially-generated parent ion and a molecule of the precursor diacetylene or cyanoacetylene. Analogous results were obtained in the vinylacetylene system, where a kinetic analysis permitted an elucidation of the structures and isomerization mechanisms of the reacting ions.

Table 1. Ion-Molecule Reaction Rate Constants and Condensation Mechanisms in the Diacetylene and Cyanoacetylene Systems.

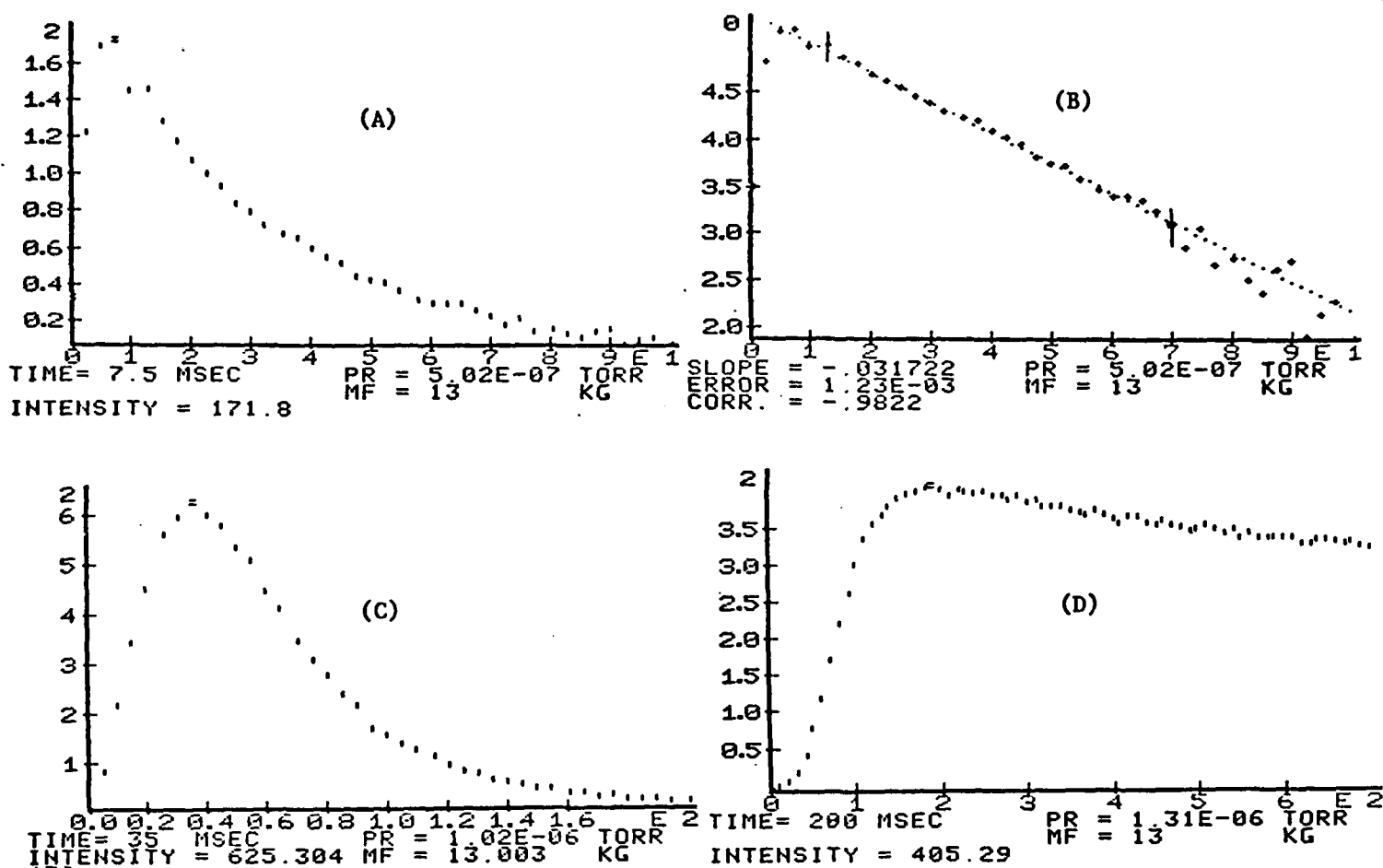| Reaction	[a]Rate Constant, cm^3/molecule-s $\times 10^{10}$
$C_4H_2^+ + C_4H_2 \rightarrow$ Products	17.$\pm$3.
$\quad \rightarrow C_6H_2^+ + C_2H_2$	
$\quad \rightarrow C_8H_2^+ + H_2$	
$\quad \rightarrow C_8H_4^+$	
$C_6H_2^+ + C_4H_2 \rightarrow$ Products	12.$\pm$8.
$\quad \rightarrow C_8H_2^+ + C_2H_2$	
$\quad \rightarrow C_{10}H_4^+$	
$\quad \rightarrow C_{10}H_2^+ + H_2$	
$C_8H_2^+ + C_4H_2 \rightarrow$ Products	6.6$\pm$1.
$\quad \rightarrow C_{12}H_4^+$	
$C_{12}H_4^+ + C_4H2 \rightarrow C_{16}H_6^+$	Not determined
$HC_3N^+ + HCCCN \rightarrow$ Products	14.$\pm$5.
$\quad \rightarrow C_4N_2^+ + C_2H_2$	
$\quad \rightarrow C_6H_2N_2^+$	
$\quad \rightarrow C_6HN_2^+ + H$	
$C_4N_2^+ + HCCCN \rightarrow$ Products	4.7$\pm$0.1
$\quad \rightarrow C_7HN_3^+$	
$C_7HN_2^+ + HCCCN \rightarrow$ Products	<0.1

[a]Error limits, 95% confidence.

Figure 1. Typical experimental results obtained in the cyanoacetylene system on the ion cyclotron resonance spectrometer. These are direct copies of the video monitor screen displaying plots of ion abundance as a function of time. With the new software developed during the last quarter, the computer automatically labels the axes and notes the experimental parameters which are displayed at the bottom of the screen.

(A) The abundance of the primary $HCCCN^+$ ion as a function of time (90 ms). This ion is generated during the 5 ms ionizing-electron pulse, and reacts at every collision with a cyanoacetylene molecule (rate constant, 17×10^{-10}).

(B) The computer replots the data from (A) on a logarithmic scale and calculates the slope, which is proportional to the rate constant.

(C) The product $C_4N_2^+$ ions formed in the reaction ($HCCCN^+ + HCCCN \rightarrow C_4N_2^+ + C_2H_2$) followed as a function of time (160 ms); note that the ion grows in and disappears more slowly than the primary ion.

(D) The unreactive product $C_7HN_3^+$ ion formed in the reaction ($C_4N_2^+ + HCCCN \rightarrow C_7HN_3^+$) as a function of time (600 ms).
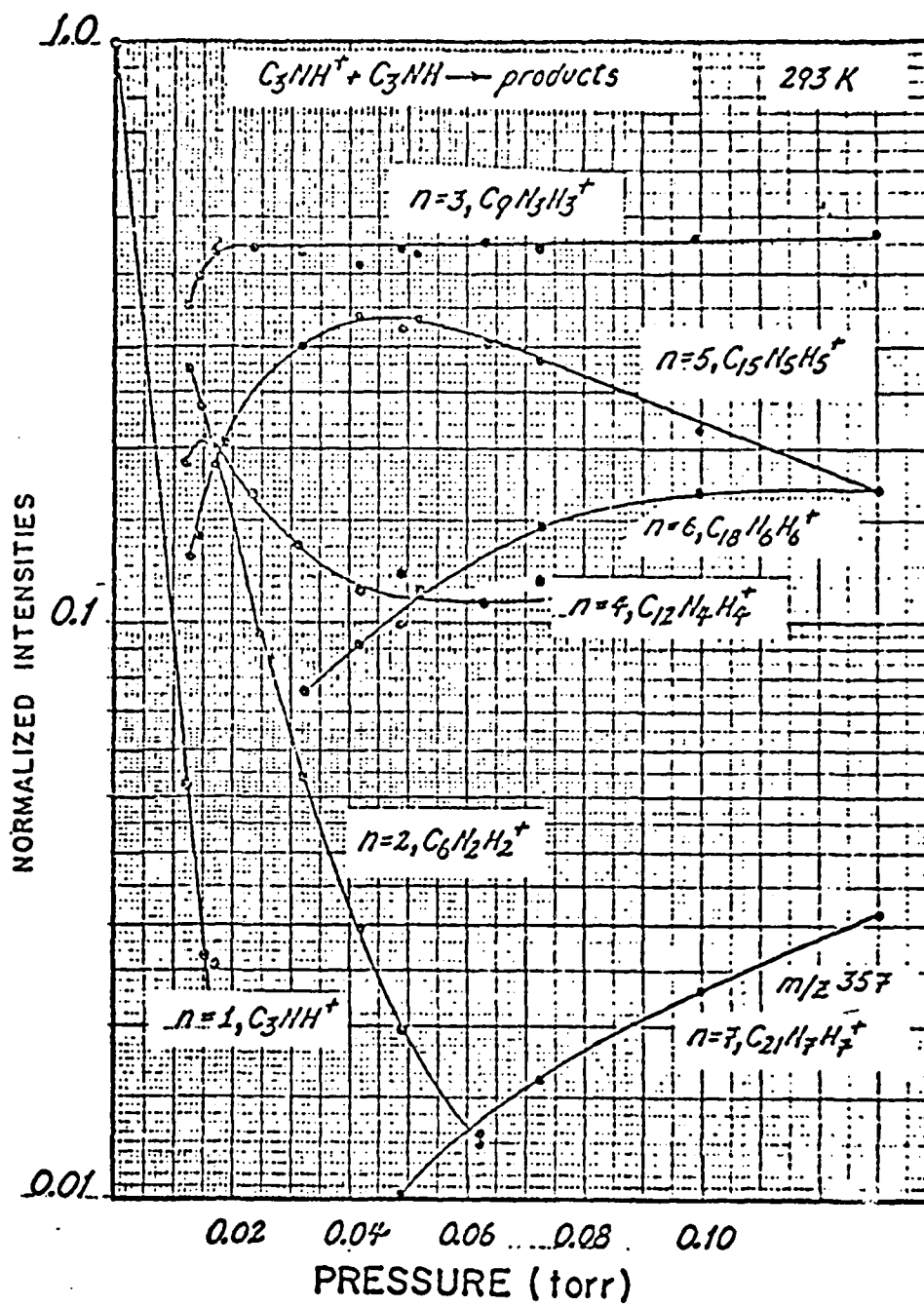
Figure 2. The abundances of positive ions formed in cyanoacetylene, as a function of pressure in the pulsed electron beam high pressure mass spectrometer.

8. Molecular Basis for Laser-Induced Vaporization of Refractory Materials

Principal Investigators: John W. Hastie, Peter K. Schenck and David W. Bonnell

Introduction

Fundamental understanding of smoke and aerosol formation from high temperature gases and vapors, formed when high-powered lasers interact with graphitic or other refractory materials, requires a molecular-level description of the vaporization/ condensation processes. In FY-83, a research program was initiated to examine this problem. The work is defined by two tasks:

Task A. Laser Vaporization Kinetics for Carbon-Containing Refractories.

Task B. Mechanisms of Formation for Submicron Metal-Containing Particulates.

Background Rationale for Task A

The ability of refractory ceramics (or related materials) to withstand very high temperatures encountered during laser heating in high vacuum space depends largely on the mechanism of ablative vaporization and the opacity of the vapor barrier produced. In principle, it should be possible to tailor the composition and structure of the ablating ceramic to optimize the vapor opacity for a particular laser radiation source. For optimum system design, a basic understanding of laser induced vaporization mechanisms, together with a knowledge of the composition (molecular species identities), spectroscopic, and electrical (ionic species identities) characteristics of the vapor phase, is needed. This understanding should also incorporate both temporally and spatially resolved information concerning species concentrations, temperatures and quantum state populations. From this type of detailed system characterization one could determine to what extent thermodynamic equilibrium, partial equilibrium, or chemical kinetics models could be applied to end-use systems. Such models would form the basis of computer codes for performance predictions of laser-ceramic interactions in a space environment.

Previous empirical experience, e.g. with thermal ablation of re-entry vehicles, has indicated the suitability of carbon producing materials for ablative heat protection. However, thermodynamic arguments suggest that much of the potential ablative cooling is lost through exothermic formation of high bond energy molecular species, C_2, C_3, C_5, etc. The internal degrees of freedom (rotational, vibrational, electronic) associated with these species may also interact with and modify electromagnetic radiation sources. It appears desirable, therefore, to modify the vaporization process to enhance carbon atom production. Inclusion of refractory transition metals (Ta, W, ...) in the solid phase should reduce the carbon thermodynamic activity through carbide formation and barrier effects and, thereby, enhance the yield of low molecular weight atomic carbon species. Similarly, addition of a few percent of metal (Ta, Hf, . . .) boride may also drastically alter the molecular distribution of carbon vapor species. This distribution could also be affected by rate processes such as laser-induced ion chemistry. For instance, the presence of even very small amounts of low ionization potential intercalated species (e.g. alkali metals such as potassium, alkaline-earth-metals such as calcium, and oxides of alkaline and rare earth metals) in graphite based ablators could be expected to produce a highly conductive plasma which can produce a strong "blanketing" effect on electromagnetic radiation. The formation of this laser-enhanced electrically conducting plasma could also alter the molecular species distribution substantially, for instance, by ion molecule reactions leading to clustering.

Approach

Thermal breakdown in vacuum of refractory metal carbides, for instance, can be expected to occur in the temperature range of 3000-5000 °C and with high local pressures ($\sim$ 1 atm). State-of-the-art experimental techniques

are needed for vapor phase composition and temperature measurement under these extreme conditions. The High Temperature Processes Group has developed many of the mass and optical spectroscopic techniques needed for a molecular specific characterization of laser plumes and high temperature vapors in general. Techniques available for this study include:

1. Very High Pressure (sampling) Mass Spectrometry (VHPMS), for quantitative measurement of molecular and ionic species concentrations in high temperature-high pressure vapors (10^{-6}-10 atm).

2. Knudsen Effusion Mass Spectrometry (KMS), for vapor pressure measurements of equilibrium systems at high temperatures and low partial pressures (10^{-8}-10^{-4} atm).

3. Transpiration Mass Spectrometry (TMS), for vapor pressure measurements of solids (or liquids) in reactive atmospheres (up to 10 atm).

4. A modified Mettler microbalance system, for Differential Thermal and Gravimetric Analysis (DTA and TGA) of refractory materials in vacuum or controlled atmospheres at high temperatures.

5. Photoelectric Pyrometry, for surface temperature measurement.

6. Laser Raman Spectrometry (LRS) for spatially resolved gas temperature measurements.

7. Laser Enhanced Ionization (LEI), for spatially resolved gas velocity measurement and ion-chemistry studies.

8. Classical absorption, emission, dye laser, infrared laser spectrometry for spectroscopic characterization of selected high temperature species.

Of these techniques, numbers 1, 3 and 7 are unique and are only available in our laboratories. A relatively few other laboratories have one or more of the remaining techniques. In addition to these experimental facilities, we also have available computer codes and data bases (unique to NBS) for thermodynamic modeling of complex multiphase non-ideal high temperature systems, of the type most likely represented by laser plumes of refractory materials.

The NBS developed VHPMS system provides sufficient pumping speed at its first stage to simulate near earth orbit vacuum conditions ($\sim 10^{-6}$ atm) even with high gas loads (> 100 cc/min). A 350 watt cw CO_2 laser is available as a heating source. Ceramic samples are mounted in the first pumping stage on a multi-axis translator to allow sampling the plume gases as a function of distance (and hence expansion time) and angle from the laser impact point. Mass spectrometric and temperature data can be obtained as a function of laser beam-surface angle. Most of the mechanistic details of the laser-vaporization process can be derived from these experiments.

Background Rationale for Task B

Fundamental understanding of smoke and aerosol formation from high temperature gases and vapors, containing inorganic species (including carbon) requires a molecular-level description of the initial process of atomic and molecular aggregation to form clusters. Experimentally, however, virtually nothing is known about inorganic clusters and their role in the homogeneous nucleation process leading to inorganic smoke. The classical theory of cluster formation and growth is based on bulk parameters, such as density

and surface tension. Under typical supersaturated conditions in high temperature vapor and combustion systems (with large temperature and species concentration gradients) the classical description suggests a critical embryo size for nucleation of 10-100 atoms. The fundamental problem with this classical approach lies in the assumption that bulk properties (density and surface tension) apply to clusters in the 10-100 atom size range. It is now recognized that this is a poor assumption and errors in predicted nucleation rates as large as a factor of 10^{20} can result with this approach. What is needed is a molecular theory which traces the step wise aggregation process and includes experimental mechanistic information and individual reaction rate constants.

Approach

Previous particle-collection and modeling studies indicate that observable cluster growth requires times of the order of $10^{-6}-10^{-3}$ sec. The low end of this time frame can be produced by nozzle expansion techniques and the high end is characteristic of nucleation times in atmospheric flames or other hot gas streams. Our VHPMS facility above provides access for both experimental approaches. The stabilized laminar flat flame (atmospheric) provides a convenient time-resolved high temperature environment for controlled cluster formation, ranging from the embryonic to dense smoke stage. Simultaneous laser optical and mass spectrometric techniques are available for monitoring the cluster growth process in atmospheric flames. The usual problems of sampling particulate-laden gas streams through molecular beam probes can be avoided by the large orifices (and hence high gas load capability) utilized by the VHPMS system.

The NBS developed technique of Transpiration Mass Spectrometry (see item 3 Task A) can be used for the production, and molecular species monitoring, of metal clusters over the 1-100 atom size range.

The general approach using these established experimental facilities is to:

(1) Adapt the VHPMS to sampling seeded flames containing clusters and particles on a millisecond time scale.

(2) Adapt laser spectroscopy and light scattering methods to the determination of cluster structure and possible size distribution up to 1 μm.

(3) Adapt the TMS technique to controlled production of clusters in expanding free jets on a microsecond time scale.

(4) Develop computer models of homogeneous nucleation based on the experimental results.

Specific problem areas in methodology development which need consideration are:

(1) Ion-precursor mass spectral assignment. This may require development of soft ionization and/or time of flight techniques.

(2) High speed-high volume data acquisition and the synchronous coupoing of mass and optical spectroscopic diagnostics. This is amenable to straight forward expansion of computer controls and data handling.

(3) Ultra high mass analysis. In the latter stages of this effort, bridging the gap between normal mass spectroscopic and light scattering particle sizes, if necessary, will require mass spectroscopic determinations of cluster entities to perhaps 100,000-150,000 atomic mass units. This is quite reasonable at the current state-of-the-art for quadrupole mass filters.

The study of cluster and particulate forming processes could also be coupled with the laser-vaporization work proposed in Task A. Laser-vaporization conditions can be set to allow cluster and particulate formation from the supersaturated vapors. This process could then be monitored using the VHPMS.

Summary of FY-83 Accomplishments for Task A

Preliminary experiments were carried out to assess the necessary laser power, beam optics, and geometric arrangements required for laser mass spectrometric measurements. A 250 watt CW CO_2 laser was used to irradiate spectroscopic grade graphite. The samples were contained in an evacuated cell (pressure $< 10^{-4}$ atm) equipped with a sodium chloride window. Total surface areas were varied from 2.4 to 8.6 cm^2. Information on the distribtuion of thermal energy in laser irradiated graphite was obtained using a 200 watt unfocused CW beam. The results indicated that tightly focused laser radiation would be required to significantly ablate graphite or similar materials. Similar tests were conducted with a 20 megawatt peak power, pulsed Nd/YAG laser system (1.06 micron), focused to a spot diamgeter of less than 250 microns with a 300 mm f/6 lens. Single pulses produced little damage, but at a 10 Hertz repetition rate, 100 pulses produced visible vapor

plumes with a surface temperature in excess of 2500 K. The visible plume extended several centimeters above the surface. These studies indicated that a réducéd laser energy, of 20 J/cm^2 from 10 mJ pulses, would suffice for the subsequent mass spectrometric measurements. Also, the vapor plume direction was observed to be normal to the sample surface and quite insensitive to the laser beam to surface angle, down to $\sim$ 30° incidence angle.

Following the laser ablation test studies, a pulsed laser system was coupled with a specially designed High Pressure Sampling Mass Spectrometer (HPMS). A schematic of the experimental arrangement is given in figure 1. Details of the mass spectrometer system, together with the principles of high pressure sampling and quantitative high temperature mass spectrometry, have been given elsewhere (Hastie and Bonnell, 1983). Basically, a molecular beam is formed from the laser plume, collimated through differentially pumped high vacuum stages, converted (in part) to singly charged positive ions by electron impact, and mass analyzed with a quadrupole mass filter.

The same high power (20 megawatt), pulsed (10 Hz) Nd/YAG laser was used for the mass spectrometric studies as for the initial ablation/vaporization tests. To reduce the laser energy to 10 mJ/pulse for the mass spectrometric measurements, the laser output frequency was doubled to 532 nm and the laser operated at near threshold. The energy delivered to the surface sample, $\leq$ 10 mJ for each 7 nsec pulse, was sufficient to vaporize graphite when focused to about 250 microns with a 500 mm f/10 lens. An increased focus, or more energy, enhanced the vaporization rate but the mass spectrometric signals decreased with time as the sample crater depth increased. Operating at lower energy and weaker focus conditions enabled us to monitor the species ablated from a single spot for over 3000 laser shots before the mass spectrometric signal levels fell to half their initial values. The sample orientation,

depicted in figure 1 was varied over the range ∂ = 15-45°, where ∂ is the tilt angle between sample surface and mount. This angle also equals that subtended by the molecular beam and the surface norm. The results of Covington et al. (1977), on the angular distribution of mass flux in plumes from laser vaporized graphite, indicate a flux reduction to 95 to 50 percent of maximum for θ = 15 to 45°. Hence the present sampling geometry allowed for analysis of the main region of the vapor plume which avoiding excessive laser excitation of the plume.

To enhance the signal to noise ratio, a 1024 channel signal averager, triggered by the laser pulse onset, was used to accumulate the history at individual atomic mass numbers. A typical channel dwell time was 5 microsecond/channel, and up to 1000 laser shots were accumulated for each mass spectral ion. An HP 9825 desktop calculator* was used to control, readout, and store the data accumulated by the averager for later transmission. High resolution plots could be made directly, and the data was transferred to an HP 9836 computer system* for further detailed analysis.

Table 1 summarizes the species detected by mass spectrometric analysis of the graphite laser plume. Several hydrocarbon species including C_2H_2 and C_4H_2 were also found. The integrated ion intensities are believed to be a good indication of the relative species partial pressures. That is, electron impact fragmentation and mass spectral sensitivity factors can be neglected to a first approximation. Future work will, however, include a detailed consideration of these factors.

A typical time-resolved averaged (200 laser shots), mass spectral signal is shown in figure 2 for C_1^+. Note that the 7 nsec laser pulse width is negligible compared to the msec time scale of figure 2. Hence the laser-on

---

* Mention of commercial items does not imply their endorsement by the U.S. Government.

and-off condition occurs effectively at the origin. The signal onset time delay of about 0.1 msec, for the case of figure 2, is attributed mainly to the flight time for the vapor beam over the 0.26 m distance from surface to ionizer. On this time scale, the time to heat the sample is negligible. The peak onset time and shape contains temperature distribution and ion precursor molecular weight information. Efforts are presently being made to deconvolute these profiles to obtain thermal information.

The multi-shot average signals shown, for instance, in figure 2, were derived from vapor which had expanded from a laser-produced crater. A typical crater size was 0.025 cm in diameter and < 0.005 cm deep. From the chronology of mass spectrometric ion intensities at a fixed sample location, we know that the first 10 to 100 shots creates a substantial amount of the crater. Future experiments are planned to monitor the crater-forming history as a function of laser pulse width, energy, and number.

The relative partial pressure data of table 1 can be subjected to a thermodynamic analysis provided the sample temperature is known. Application of optical temperature measurement techniques have been deferred owing to uncertain emissivity data. Based on our earlier experience with high pressure sampling mass spectrometry, together with the associated gas dynamic theory, the beam composition represents a "frozen equilibrium" of the pre-expansion temperature and pressure condition (Hastie, 1974; Bonnell and Hastie, 1979). Hence surface temperatures may be derived from a comparison of the experimental "frozen" beam composition with the known thermodynamic data. Such an analysis was performed using the C_n^+/C_3^+ ratios in comparison with the results given by JANAF (1971). The results of this analysis are summarized in table 1. Note that the temperatures deduced are about the same for 26 and 96 eV ionizing

energies for each of the observed C_n^+ species. The average temperature of 4200 ± 200 K obtained from C_4 and C_5 is consistent with literature reports (e.g., see Zavitsanos, 1968). Also, the uncertainty of ± 200 K is comparable with that of earlier work. The apparent temperatures calculated from the C_1 and C_2 data can readily be accounted for by reasonable estimates of ionization cross section (σ) and sensitivity factors. For instance, the C_2/C_3 data would yield a 4200 K temperature if the relative σ's were 1/1.5, which is reasonable based on empirical trends for other systems. This ratio compares reasonably with the estimate of 1/1.23 given by Meyer, et al. (1973). It is also pertinent to note that the present graphite system appears to be very close to equilibrium and is not controlled by surface kinetics and low vaporization coefficients, contrary to earlier work. This observation is attributable to the signal averaging of a large number of laser shots, most of which impact within a crater which serves as a crude Knudsen cell.

Additional laser-induced vaporization measurements and a more detailed analysis of the graphite system will be made in FY-84. Also the pulsed Nd/YAG laser systems will be replaced with a more versatile Nd/YAG system. This new system will allow for improved control over pulse energy and duration and will operate at twice the pulse rate (20Hz) with improved beam quality.

Similar studies with metal carbide materials are also planned and we have prepared hot pressed samples of TaC for this purpose. We expect TaC to differ from graphite in its vaporization kinetics and speciation. Inconclusive literature evidence exists for either C atoms or C_2 molecules to be the predominant vapor species over TaC.

Summary of FY-83 Accomplishments for Task B

The free-jet expansion method of cluster formation was tested using KCl vapor species. For this purpose, the transpiration mass spectrometric apparatus was used (Bonnell and Hastie, 1979). The results have been presented in detail in the manuscript "Transpiration Mass Spectrometric

Analysis of Liquid KCl and KOH Vaporization" by J. W. Hastie, K. F. Zmbov and D. W. Bonnell, to appear in the journal High Temperature Science. As a corollary to this study, the analysis of cluster formation was complicated by an unusual temperature dependence of the electron impact ionization process. This problem will be addressed in FY-84 under the new Task C, as detailed in our proposal document.

References

Bonnell, D. W. and Hastie, J. W., (1979), Proc. 10th Matls. Res. Symp. NBS SP-561, p. 357.

Covington, M. A., Liu, G. N. and Lincoln, K. A., (1977). AIAA J. 15, 1174.

Hastie, J. W., (1974), Int. J. Mass Spec. and Ion Phys., 16, 89.

Hastie, J. W. and Bonnell, D. W., (1983), "Transpiration Mass Spectrometry-- A New Thermochemical Tool," in Thermochemistry Today and Its Role in the Immediate Future, Ribeiro da Silva, M. A. V., ed., Reidel Publ., Boston.

JANAF, (1971), JANAF Thermochemical Tables, Stull, D. R. and Prophet, H., NSRDS-NBS 37.

Meyer, T. R., Lynch, A. W. and Freese, J. M., (1973), J. Phys. Chem. 77, 1083.

Zavitsanos, P. D., (1968), Carbon 6, 731.

Table 1. C_n Ion Intensities and Corresponding Equilibrium
Surface Temperatures[a]

Mass (amu)	Species	Peak Signal	Integrated Signal	Temperature (K)[b]
Ionizing electron energy = 96 eV				
12	C_1	0.51	0.32	2600
24	C_2	0.16	0.12	3450
36	C_3	1.0	1.0	---
48	C_4	0.015	0.018	4400
50	C_5	0.04	0.04	4300
Ionizing electron energy = 26 eV				
12	C_1	0.47	0.32	2600
24	C_2	0.14	0.11	3200
36	C_3	1.0	1.0	---
48	C_4	0.014	0.013	4100
50	C_5	0.027	0.027	4000

[a]The accuracy of the C_1 and C_2 ratios to C_3 is about 10 percent which
corresponds to about ± 300 K; for C_4 and C_5 the accuracy is about 25 percent.
Typical C_3 signals are 100 to 200 mv peak.

[b]Obtained by comparison of observed Integrated Signal intensities, relative
to C_3, with the JANAF (1971) thermochemical partial pressure data.

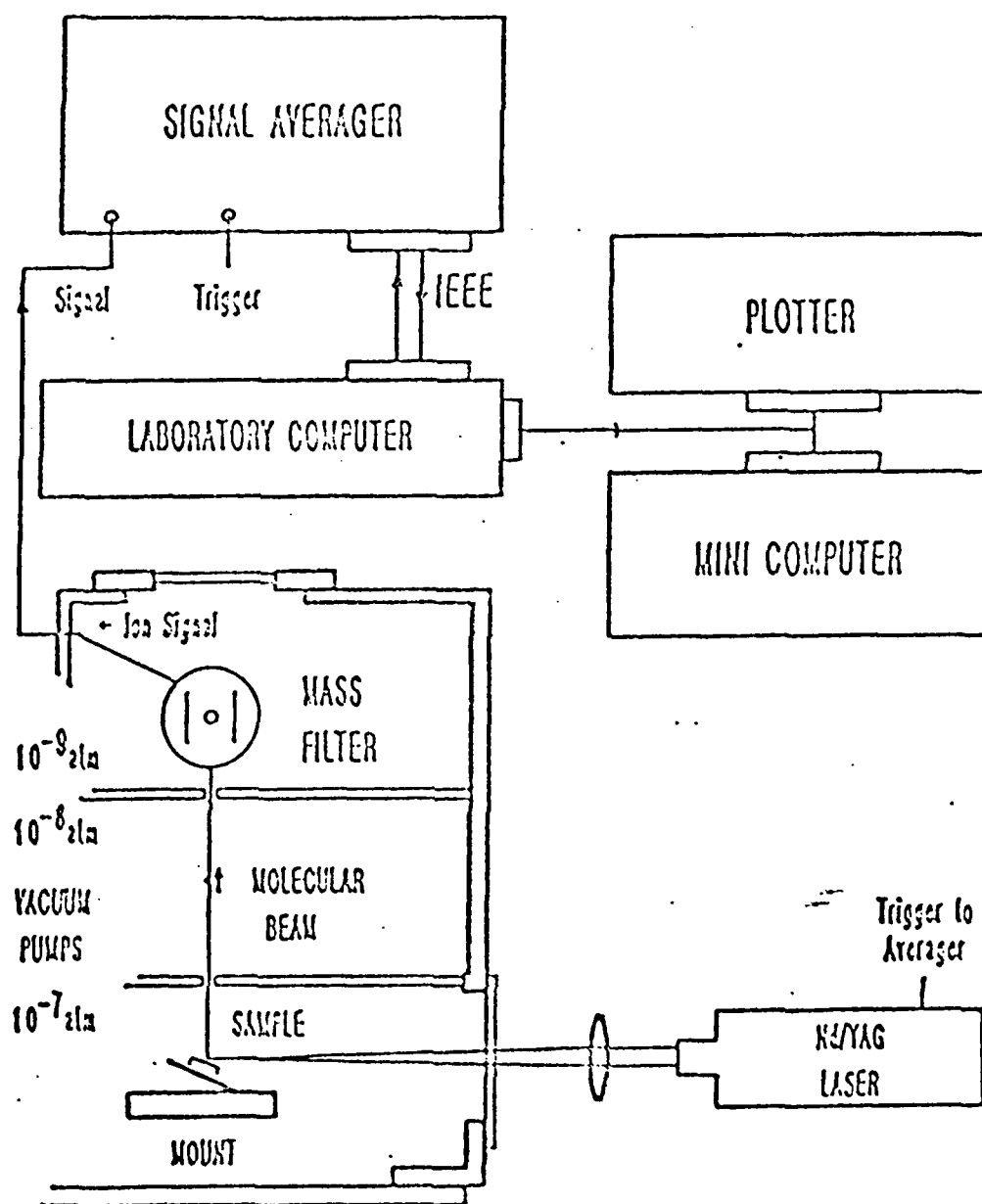# LASER VAPORIZATION MASS SPECTROMETER

Figure 1. Schematic of laser vaporization-mass spectro-
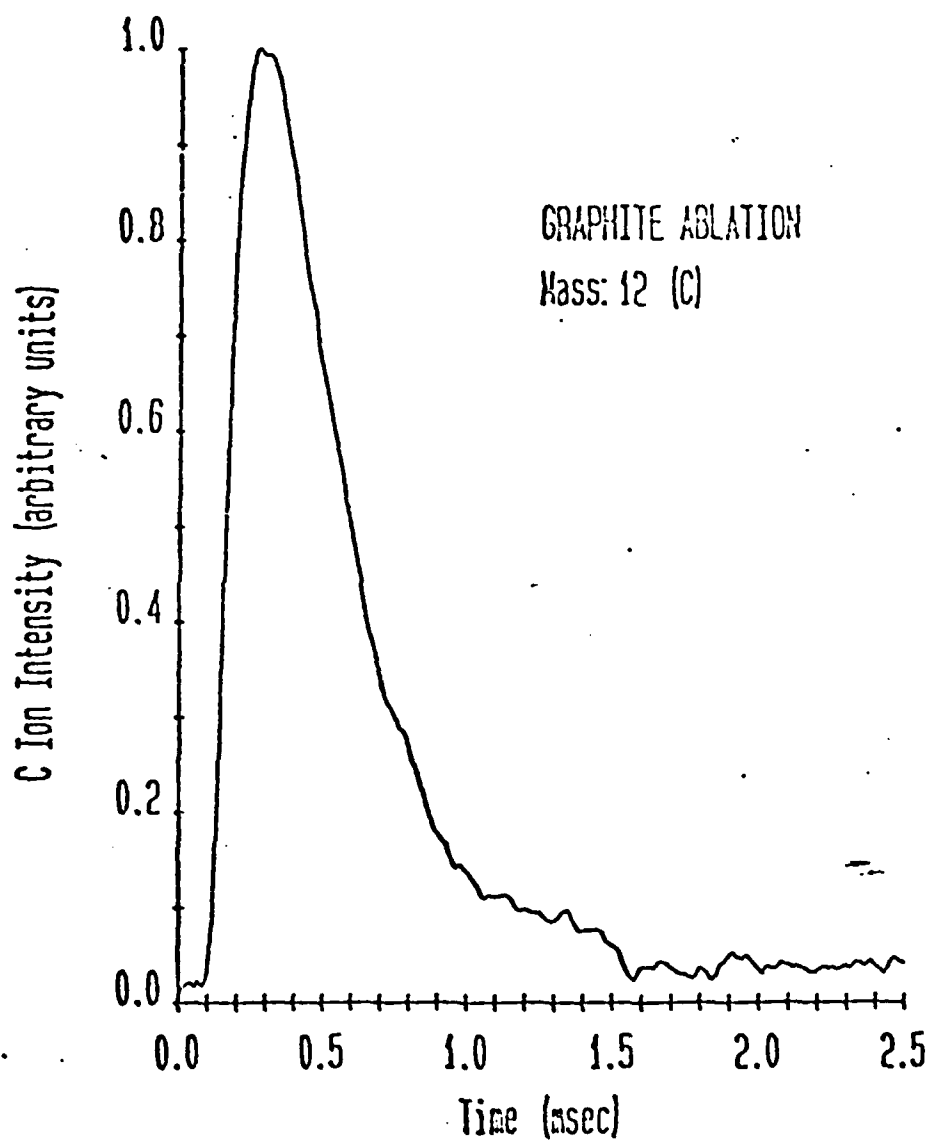metric facility.

Figure 2. Time resolved profile of C^+ (C atom precursor) produced by laser-induced vaporization mass spectrometry of graphite at ~ 4200 K.

END

FILMED

12-84

DTIC